NASA TECHNICAL NOTE

NASA TN D-3103

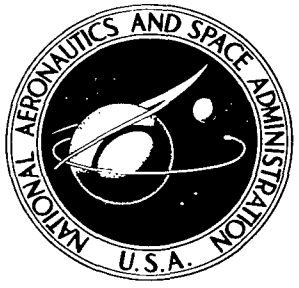

ANALYSIS OF LOW-TEMPERATURE DIRECT-CONDENSING VAPOR-CHAMBER FIN AND CONDUCTING FIN RADIATORS

by Henry C. Haller, Bruce G. Lindow, and Bruce M. Auer

Lewis Research Center
Cleveland, Ohio

NATIONAL AERONAUTICS AND SPACE ADMINISTRATION - WASHINGTON, D. C. - NOVEMBER 1965

ANALYSIS OF LOW-TEMPERATURE DIRECT-CONDENSING VAPOR-CHAMBER FIN AND CONDUCTING FIN RADIATORS

By Henry C. Haller, Bruce G. Lindow, and Bruce M. Auer

Lewis Research Center
Cleveland, Ohio

NATIONAL AERONAUTICS AND SPACE ADMINISTRATION

For sale by the Clearinghouse for Federal Scientific and Technical Information
Springfield, Virginia 22151 – Price $3.00

CONTENTS

ANALYSIS OF LOW-TEMPERATURE DIRECT-CONDENSING VAPOR-CHAMBER FIN AND CONDUCTING FIN RADIATORS

by Henry C. Haller, Bruce G. Lindow, and Bruce M. Auer

Lewis Research Center

SUMMARY

An analytical comparison of flat, direct-condensing finned-tube space radiators employing vapor-chamber, double, and central fin-tube geometries was made for a low power output, low-temperature Rankine space power electric generating system. The descriptive equations for the radiator investigation included in addition to the heat-transfer analysis, consideration of vapor and liquid headers, pressure drop in the headers and radiator tubes, meteoroid protection for the tubes, headers, and vapor-chamber fins, and temperature drop in the tube armor. The heat-transfer, weight, and geometry characteristics of the three radiator fin-tube configurations were determined over a wide range of variables for design conditions descriptive of a 30-kilowatt powerplant that used steam as the thermodynamic cycle fluid. The thermal degradation of the vapor-chamber fin-tube radiator due to puncture of the individual fin segments, and the vapor chamber heat transfer and capillary fluid flow requirements were also investigated.

For the example case chosen, which employed a tube meteoroid nonpenetration probability of 0.90, the vapor-chamber fin radiator was clearly not superior in heat rejection per unit weight to the central and double fin geometries. The largest values of heat rejection per unit weight were obtained for the double-fin geometry radiator.

For a tube nonpenetration probability of 0.995, the vapor-chamber fin radiator had a substantially greater heat rejection per unit weight compared to the central fin-tube radiator (80 to 130 percent increase) over the entire range of tube inner diameters from 0.075 to 0.375 inch. For a ratio of tube block sidewall thickness to full armor thickness equal to 0.5, the vapor-chamber fin radiator was also substantially better than the double-fin radiator (order of 20 to 70 percent greater in maximum heat rejection per unit weight). It was only for the case of ratio of sidewall thickness to armor thickness approaching zero that the vapor-chamber fin radiator was not superior to the double fin radiator.

Radiator geometry considerations indicated, that at the minimum weight condition, the vapor-chamber fin-tube radiator had a substantially smaller planform area (20 to 40 percent), fewer radiator tubes, and larger tube inner diameters than the other two fin-tube geometries. The double fin-tube radiator at minimum weight has a major disadvantage because the fins are very thin thus posing possible fabrication and structural problems.

INTRODUCTION

Heat rejection to space from electric power generating systems operating at relatively low cycle temperatures requires radiators of large planform area. Radiators designed for the rejection of waste heat generally employ fins as extended radiation heat-transfer surfaces between fluid-carrying tubes. Such an arrangement reduces the amount of the overall radiator surface occupied by flow passages and thereby reduces the area vulnerable to critical damage from impacting meteoroids.

The central fin-tube geometry, which consists of a number of parallel tubes separated by solid fins located in the plane of the tube centers, is often considered. Analyses of the solid-conducting central fin-tube radiators are given in references 1 to 6. Other solid-conducting fin-tube arrangements, such as the double fin-tube and open sandwich fin-tube radiators, are analyzed in references 7 and 8.

In order to find a means of increasing the radiating effectiveness of the solid fin radiators along with decreasing weight and planform area, the vapor-chamber fin-tube concept was analyzed and compared to the central and double fin-tube geometries for high-power-level, high-temperature-level radiators in reference 9. The vapor-chamber fin concept proposes to reduce radiator weight and area by providing for an essentially isothermal fin between tubes: the single solid fin is replaced by a double-wall fin that forms a hollow chamber between tubes. A working fluid in the chamber can then be boiled off the tube surfaces and condensed on the fin surfaces to produce a fin of constant temperature and high radiating effectiveness. Condensate is then returned to the boiling surface by capillary pumping, which is essentially insensitive to gravity (ref. 10).

The results of reference 9 indicate that the vapor-chamber fin-tube radiator concept results in a sizable weight advantage over both the central fin-tube and the double fin-tube configurations at high power and temperature levels. The vapor-chamber fin-tube radiator was also shown to have a substantially smaller planform area, fewer number of radiator tubes, and larger tube inner diameters at minimum weight than the other two fin-tube geometries.

This investigation was made to see if the relative advantages obtained for the vapor-chamber fin radiator in a high-temperature, high-power-level system (ref. 9) also hold at low power and temperature levels. In order to carry out this objective, numerical calculations were conducted for the three fin-tube geometries as planer direct-condensing radiators employing design inputs characteristic of a 30-kilowatt Rankine electric power-generating cycle using steam as the working fluid. Radiator heat transfer, weight, and geometry characteristics were determined for a wide range of variables such as tube inside diameter, fin profile ratio, ratio of tube-block sidewall thickness to armor thickness in the case of the double and vapor fin-tube geometries, conductance parameter for the solid fin radiators, fin vapor-chamber boiling heat-transfer coefficient, ratio of boiling to condensing heat-transfer coefficients for the vapor-chamber fin, vapor-chamber fin

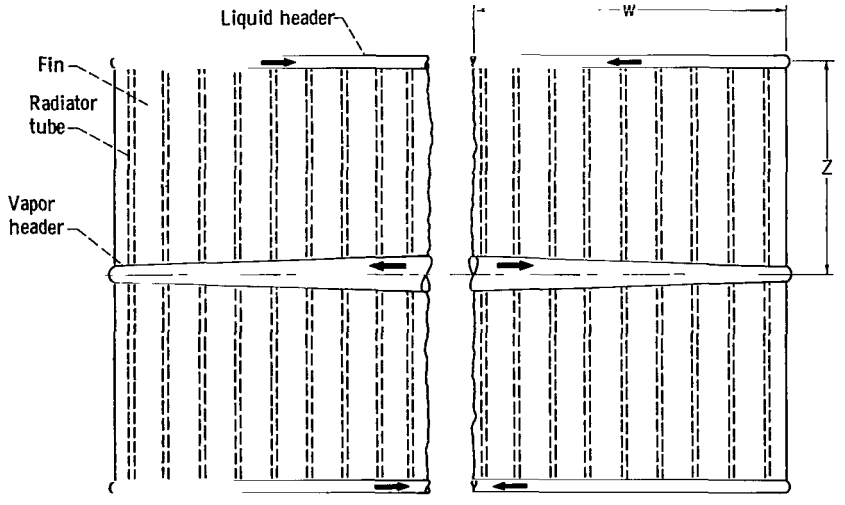

Figure 1. - Four-panel fin-tube radiator.

capillary mechanism weight, and vapor-chamber fin segment planform area.

The vapor-chamber fin-tube configuration was initially investigated to determine major influencing factors and to establish representative conditions for comparison with the other fin-tube geometries. Boiling heat flux and capillary flow requirements for the vapor-chamber fin were also determined. In addition, the one-dimensional radiating effectiveness of a punctured segment of a vapor-chamber fin, which then acts as a solid-conducting fin, was determined to indicate the maximum loss in effectiveness that might be encountered with this configuration.

The two solid-conducting fin radiators were investigated and then compared with the vapor-chamber fin-tube radiator over the same range of tube inner diameters for the same materials, cycle conditions, tube and header pressure drops, and meteoroid protection criteria

ANALYSIS

Radiator Configuration

The general radiator panel configuration considered for the analysis is shown in figure 1. The configuration illustrated is a flat plate direct-condensing radiator that radiates hemispherically to space from both sides and is applicable to Rankine power cycles. Exhaust from the cycle turbine is distributed to the finned tubes by the central vapor header. The heat radiated from the vapor header and finned tubes causes the vapor to condense. The condensate is then subcooled and collected in the outer liquid headers before being sent to the condensate pump.

The vapor header is assumed to be a hollow paraboloid whose wall consists of a 0.030 inch liner and meteoroid protection armor of the same thickness as that required

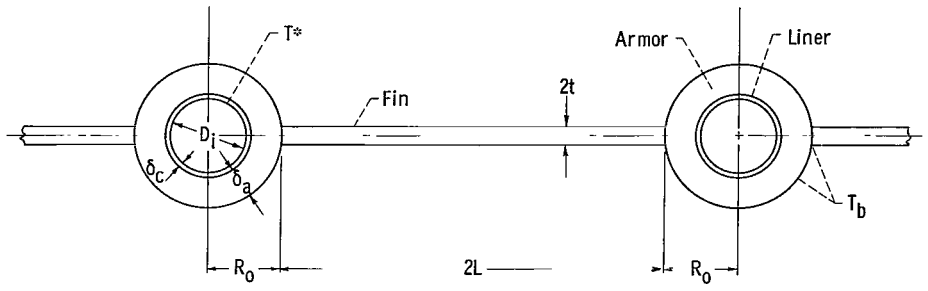

(a) Central fin-tube configuration.

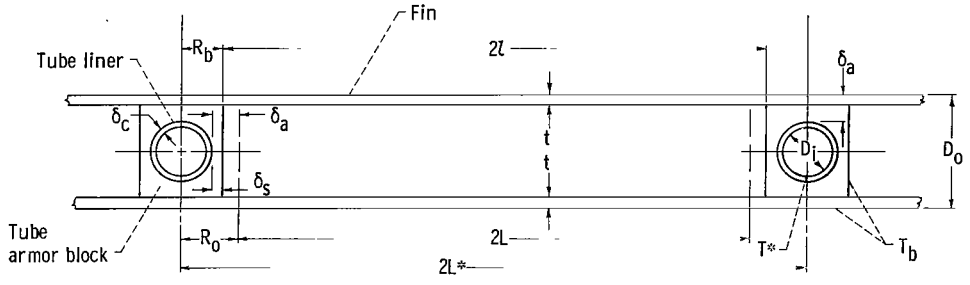

(b) Double fin-tube with variable tube-block sidewall thickness.

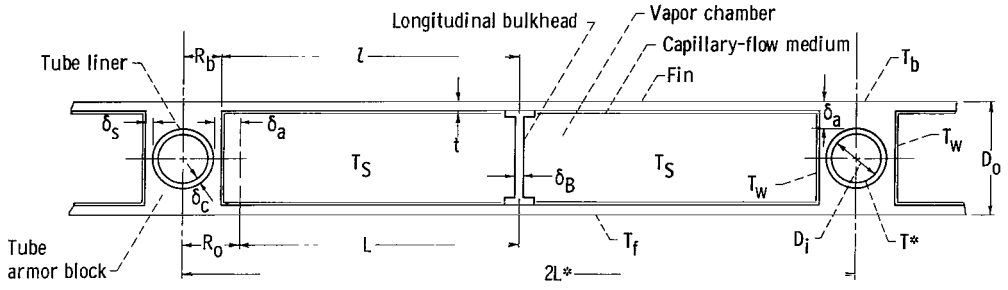

(c) Vapor chamber fin-tube with variable tube block sidewall thickness.

Figure 2. - Cross sections of radiator fin-tube configurations.

by the tubes. The parabolic shape is intended to produce a constant velocity in the header. For simplicity, the liquid header was designed with a constant diameter at a prescribed fluid pressure drop. The liner for the liquid header has the same thickness as the tube liners (0.020 in.) and is independent of header diameter. The liquid header also has meteoroid armor thickness equal to that obtained for the tubes. No heat radiation or subcooling is credited to the liquid header.

Solid fin geometries. - The detailed cross-sectional drawings of the three geometries to be compared are shown in figure 2. The central fin tube geometry of figure 2(a) consists of a rectangular fin attached to two round tubes in which a liner is inserted.

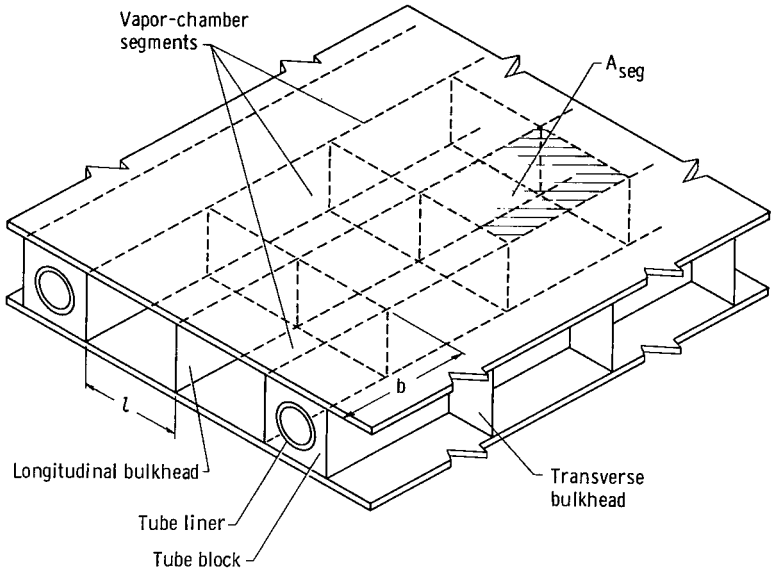

Figure 3. - Isometric drawing of vapor-chamber fin-tube configuration.

The double fin-tube with variable tube sidewall thickness δ_s is composed of a tube liner inserted in an armor block to provide meteoroid protection and two rectangular fins (fig. 2(b)). (Symbols are defined in appendix A.) This geometry offers some advantages because it can act as a bumper screen that will afford protection against meteoroid impact damage on the tube block sidewalls.

Vapor-chamber fin geometry. - The vapor-chamber fin-tube geometry of figure 2(c) consists of a tube liner inserted in an armor block to provide meteoroid protection and two rectangular fins forming a sealed, enclosed chamber between adjacent tubes. A capillary flow medium such as narrow grooves, woven wire mesh, or fibrous matt lines the inner surfaces of the fin chamber and is saturated with a heat-transport fluid. The fluid used should provide a saturation pressure at the chamber operating temperature that is compatible with the chamber construction.

Inasmuch as the vapor chamber will lose its heat-transport action if a puncture and loss of transport fluid occurs, the long fin chambers are divided into a number of sealed compartments by a longitudinal and numerous transverse bulkheads (fig. 3) in order to localize the effect of a puncture. The thickness for both longitudinal and transverse bulkheads was taken as 0.020 inches. The exposed area of each compartment A_{seg}, which determined the total number of fin compartments N, was designated an independent variable. The thickness of the fin t was based on a given probability that a certain percentage of the compartments would remain unpunctured at the end of the design lifetime of the radiator. The actual dimensions of the fin result from an optimization procedure that includes meteoroid protection considerations for the fin. The calculation procedure of reference 11 is used for the meteoroid puncture criterion with vulnerable area taken

to be the exposed surface of a fin segment.

Meteoroid damage. - For the vapor fin geometry and the double fin geometry, the liner can be damaged by impacting meteoroids in two general ways. The first is by any primary impacts occurring on the outer exposed surfaces of the tube block. These impacts are assumed to obey the conventional armor penetration and damage relations developed for tubes. Accordingly, the tube armor block thickness δ_a was determined by using the criterion of reference 11 in conjunction with a vulnerable area given by $4R_bZN_T$. The armor thickness, which is a result of the optimization program, is applied in full on the upper and lower surface of the tube (figs. 2(b) and (c)).

A second damage source can arise from a spray of particles on the tube block sidewall $2(R_o - t)ZN_T$ resulting from impacts on the fin surfaces. In view of the bumper action involved, however, and the obliquity of the secondary impacts, a reduction will undoubtedly be allowed in the armor thickness required by the tube block sidewall to resist the effects of these secondary impacts. Since precise relations are at present unavailable for the determination of this sidewall thickness, a parametric variation of the ratio δ_s/δ_a is used to permit examination of the effects of reduced sidewall thickness on radiator weight and geometry.

Design Conditions

Design conditions for the three radiator configurations were taken as representative of a 30-kilowatt steam Rankine cycle. The cycle chosen had a peak turbine inlet temperature of 1660° R and a fluid temperature of 830° R at the radiator inlet. The total heat rejection load for the radiator was 7.5×10^6 Btu per hour. The cycle fluid entered the radiator with a quality of 100 percent and a flow rate of 0.24 pounds per second. It was also specified that the radiator tubes would subcool the working fluid 16° R. Reference 12 was used to obtain additional cycle factors such as turbine and generator efficiencies, which were set at 0.56 and 0.85, respectively, with 10 percent of the generator output required for accessories and controls. The emittance of the radiator surface was taken to be 0.90, and the effective sink temperature of space was assumed to be 0° R in order to utilize available high-temperature computer program routines. The assumption of a zero effective sink temperature results in about a 5 percent reduction in radiator area compared to the area required for a typical effective sink temperature of 400° R.

Calculation Procedure and Inputs

Calculations employing the results of the thermal analysis (appendixes B and C)

along with the weight and geometry equations (appendix D) were performed for the three radiator geometries using an iterative procedure programmed into an electronic digital computer (ref. 4). Program inputs required were tube internal diameter, radiator vapor inlet temperature, cycle power level and conditions, properties of materials of construction and cycle fluid, meteoroid protection criterion, along with the various geometric and fin heat-transfer parameters for the three geometries.

The tube armor and fin were taken to be aluminum, and the tube liner was prescribed to be stainless steel. Radiator material properties were assumed constant with temperature and evaluated at the radiator inlet temperature. Properties used for the aluminum fin and armor were a material density of 169 pounds per cubic foot, a thermal conductivity of 112 Btu/(hr)(ft)(^{o}F), and a modulus of elasticity of 0.1397×10^{10} pounds per square foot. The stainless-steel liner density was taken as 500 pounds per cubic foot.

All three radiator configuration calculations used the same inputs of material constants, thermodynamic cycle inputs, meteoroid protection criteria, pressure drops in the tubes and headers, and cycle fluid properties. A 500-day mission time and probability of no puncture $P(0)_t$ of 0.90, 0.95, and 0.995 were chosen for the calculation of the tube and header meteoroid protection thickness.

For the segmented vapor-chamber fins, a probability of $S = 0.90$ was specified so that 25 percent of the fin segments would be punctured in the lifetime of the radiator. An additional case investigated specified that 50 percent of the fin segments were punctured.

Two values of the ratio of tube sidewall thickness to tube armor thickness were used for both the vapor-chamber and double fin-tube radiators ($\delta_s/\delta_a = 0$ and 0.5). The vapor-chamber fin segment planform areas were set at 20, 40, 80, and 120 square inches. Vapor-chamber boiling heat-transfer coefficients and the ratio of the boiling to condensing heat-transfer coefficients were also parametrically varied, and two values of vapor-chamber capillary material weight were assumed.

The radiator inlet pressure was 186 psia with a ratio of total pressure drop to total inlet pressure for the entire radiator set at 0.11. This pressure drop was composed of $\Delta P/P = 0.02$ for the vapor header, $\Delta P/P = 0.07$ for the radiator tubes, and $\Delta P/P = 0.02$ for the liquid header. Included in the tube pressure drop was the turning loss and acceleration pressure drop from the vapor header to the tubes. The minimum weights obtained from the radiator optimization along with the resultant geometry were determined for a range of tube inside diameters from 0.075 to 0.375 inch.

VAPOR-CHAMBER FIN-TUBE CHARACTERISTICS

Radiator Weight

The vapor chamber fin radiator heat rejection per unit weight Q_{rej}/W was calculated for a range of values of tube inside diameter D_i, tube sidewall ratio δ_s/δ_a, boiling heat-transfer coefficient h_B, fin segment planform area A_{seg}, ratio of the number of surviving to design fin segments N_s/N, and capillary material weight $\overline{\rho_w \delta_w}$ over a range of the parameter L/R_o.

Sample results showing the variation in heat rejection rate per unit weight as a function of the L/R_o ratio for two values of tube-block sidewall thickness ratio, and boiling heat-transfer coefficient are plotted for representative conditions in figure 4. Each curve at constant h_B is seen to peak at a specific value of L/R_o. The value of Q_{rej}/W increases as the boiling heat-transfer coefficient increases since larger values of h_B and h_C allow a higher average fin temperature (appendix C). The value of L/R_o at peak Q_{rej}/W decreases substantially as the value of h_B is decreased, while a small decrease in Q_{rej}/W occurs when the tube-block sidewall thickness ratio is increased from 0 to 0.5 for both values of h_B. The cycle vapor velocity at the inlet to the radiator tubes was on the order of 100 feet per second, but the two-phase flow still remained turbulent-turbulent as considered in the pressure drop analysis (appendix E).

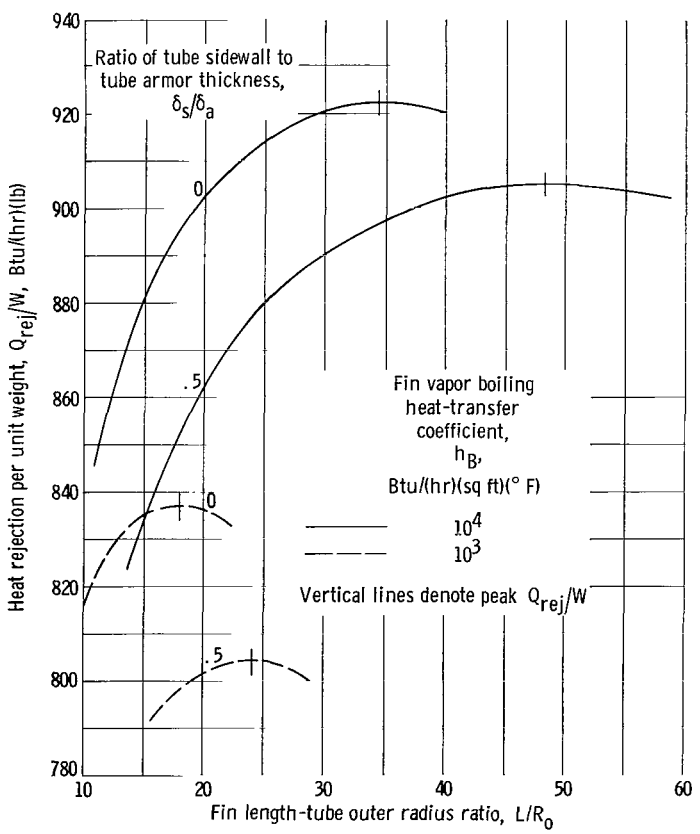

Figure 4. - Variations of heat rejection per unit weight with fin length-tube outer radius ratio for vapor-chamber fin-tube radiator. Fin segment planform area, 80 square inches; tube inside diameter, 0.15 inch; capillary weight, 0.1 pound per square foot; ratio of fin vapor boiling to fin vapor condensing heat-transfer coefficient, 1.0; tube-header nonpenetration probability, 0.90; ratio of surviving segments to total fin segments, 0.75.

Values of the maxima for each constant h_B curve (peak Q_{rej}/W) for the two values of δ_s/δ_a of figure 4 along with comparable results for other tube inside diameters are shown plotted in figure 5. According to figure 5, a sizable variation in the choice of tube inside diameter can be afforded with little reduction in the value of Q_{rej}/W because of the flatness of the curves near the peak values. It is also noted that decreasing the value of N_s/N to 0.5 results

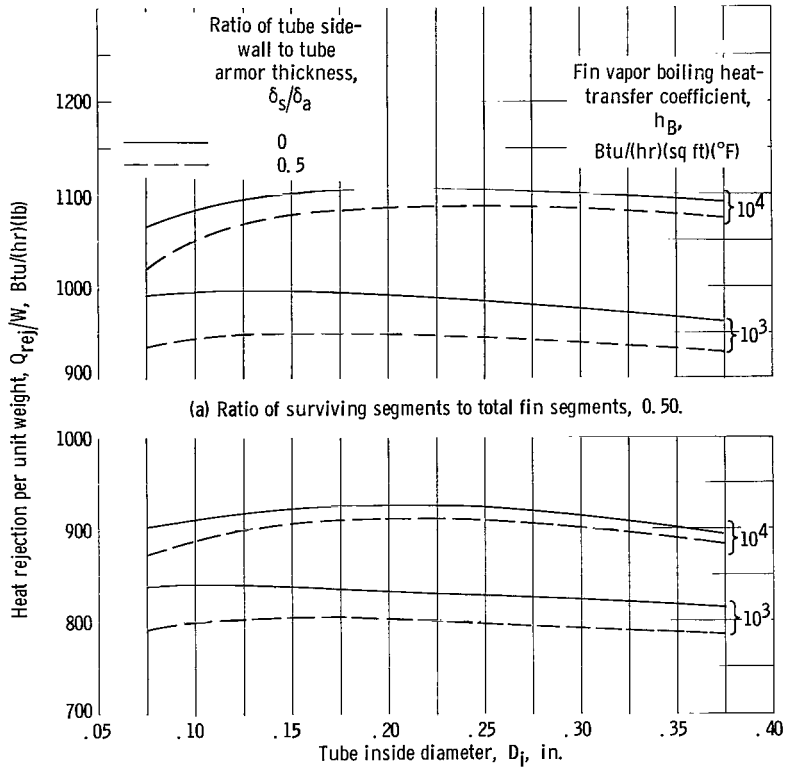

(a) Ratio of surviving segments to total fin segments, 0.50.

(b) Ratio of surviving segments to total fin segments, 0.75.

Figure 5. - Vapor-chamber fin-tube radiator peak heat rejection per unit weight. Fin segment planform area, 80 square inches; capillary weight, 0.10 pound per square foot; ratio of fin vapor boiling to fin vapor condensing heat-transfer coefficient, 1.0.

in about 18 percent higher values of Q_{rej}/W because of a smaller fin thickness involved.

A substantial reduction in Q_{rej}/W occurs when the value of the fin segment planform area is increased as shown in figure 6. The maximum Q_{rej}/W for each choice of A_{seg} was obtained from plots of peak Q_{rej}/W against tube inside diameter similar to the results shown in figure 5. The reductions in maximum Q_{rej}/W are brought about because the individual fin segment nonpenetration probability $P(0)_f$ increases as the fin segment area increases (for a fixed overall nonpuncture probability S), which results in an increased fin chamber wall thickness and increased fin weight. The relative reductions in maximum Q_{rej}/W with increasing A_{seg} are about the same for the range of the parameters h_B, δ_s/δ_a, or N_S/N considered. From a weight point of view it would seem that A_{seg} should be small; however, this leads to a large number of fin segments.

The effect of varying the fin chamber capillary material weight on the radiator maximum heat rejection per unit weight is shown in figure 7. For the range of values $\overline{\rho_w \delta_w}$ considered, sizable reductions in maximum Q_{rej}/W occur as the magnitude

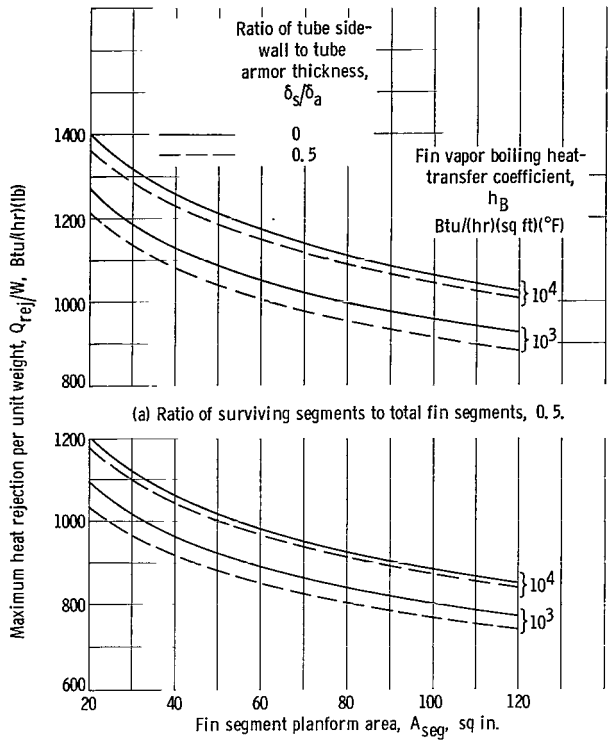

(a) Ratio of surviving segments to total fin segments, 0.5.

(b) Ratio of surviving segments to total fin segments, 0.75.

Figure 6. - Vapor-chamber fin-tube radiator maximum heat rejection per unit weight plotted against fin segment planform area. Capillary weight, 0.1 pound per square foot; ratio of fin vapor boiling to fin vapor condensing heat-transfer coefficient, 1.0; tube-header nonpenetration probability, 0.90.

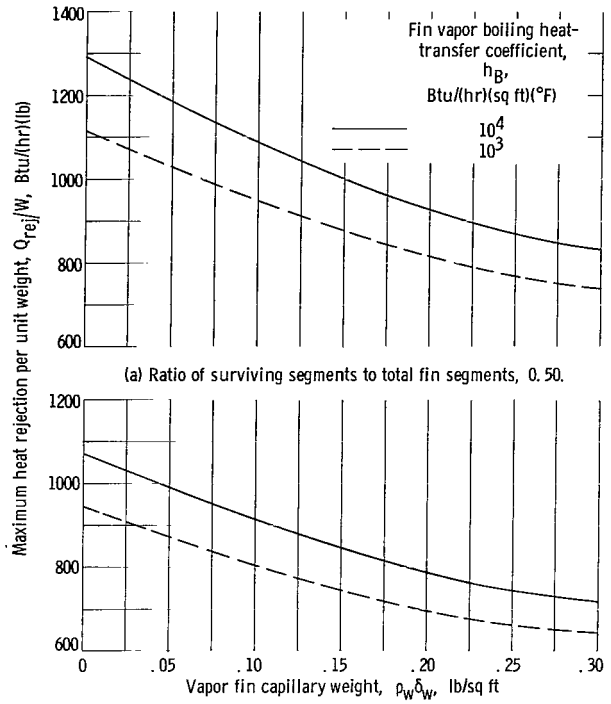

(a) Ratio of surviving segments to total fin segments, 0.50.

(b) Ratio of surviving segments to total fin segments, 0.75.

Figure 7. - Effect of vapor-fin capillary weight on maximum heat rejection per unit weight. Fin segment planform area, 80 square inches; ratio of fin vapor boiling to fin vapor condensing heat-transfer coefficient, 1.0; tube-header nonpenetration probability 0.90; ratio of tube sidewall to tube armor thickness, 0.5.

of $\overline{\rho_w\delta_w}$ increases. The relative reductions in maximum Q_{rej}/W with $\overline{\rho_w\delta_w}$ are about the same for a wide range of the other fin chamber parameters (h_B, δ_s/δ_a, and N_s/N).

Radiator Geometry

Planform area. - The planform area of the vapor-chamber fin-tube geometry at peak Q_{rej}/W is shown plotted against tube inside diameter in figure 8 for two values of h_B. Increasing the boiling heat-transfer coefficient h_B is the prime factor in reducing the planform area over the entire range of tube inside diameters investigated. This results from the strong dependence of fin surface temperature on the heat-transfer coefficients. The radiator planform area increases as the tube inside diameter is increased for the $h_B = 10^3$ case but tends to become flat for the $h_B = 10^4$ case. Variations of the tube sidewall ratio δ_s/δ_a and the ratio of surviving segments to total fin segments N_s/N resulted in small variations in planform area.

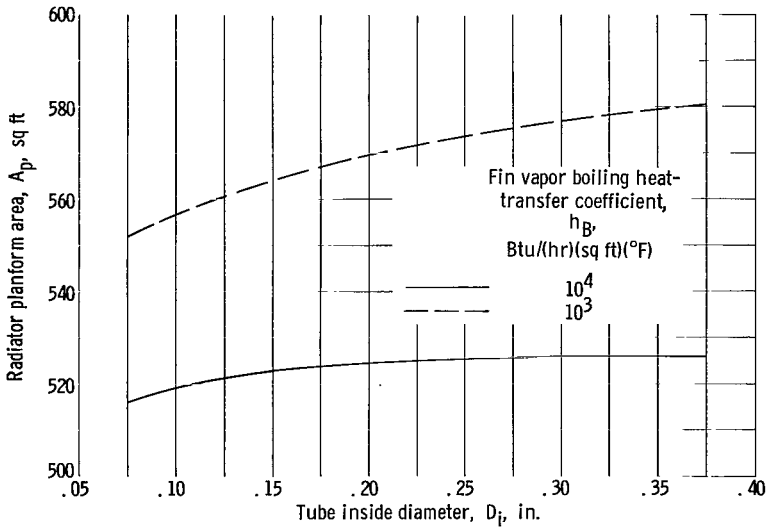

Figure 8. - Variation of vapor-chamber fin-tube radiator planform area with tube inside diameter. Fin segment planform area, 80 square inches; capillary weight, 0.1 pounds per square foot; ratio of fin vapor boiling to fin vapor condensing heat-transfer coefficient, 1.0; tube-header nonpenetration probability, 0.90; ratio of surviving segments to total fin segments, 0.75; ratio of tube sidewall to tube armor thickness, 0.5.

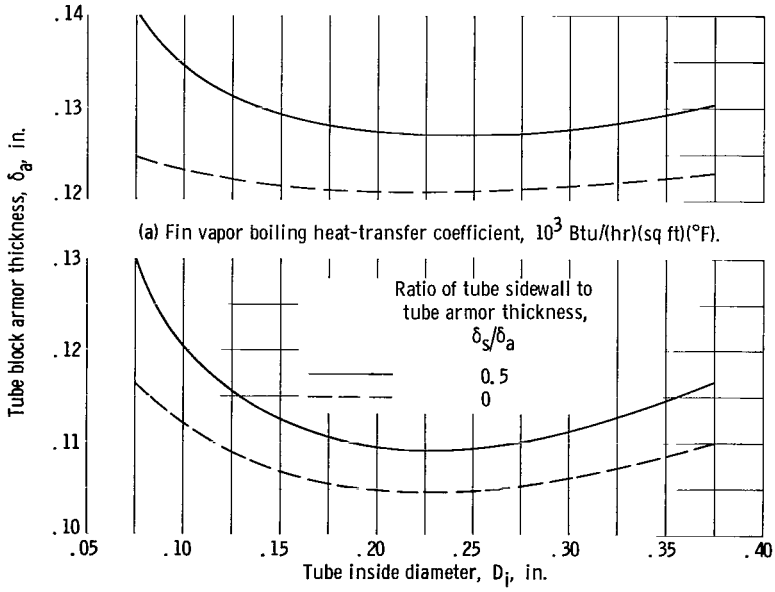

(a) Fin vapor boiling heat-transfer coefficient, 10^3 Btu/(hr)(sq ft)(°F).

(b) Fin vapor boiling heat-transfer coefficient, 10^4 Btu/(hr)(sq ft)(°F).

Figure 9. - Variation of tube block-armor thickness at peak heat rejection per unit weight with tube inside diameter vapor-chamber fin tube radiator. Fin segment planform area, 80 square inches; capillary weight, 0.1 pounds per square foot; ratio of fin vapor boiling to fin vapor condensing heat-transfer coefficient, 1.0; tube-header nonpenetration probability, 0.90; ratio of surviving segments to total fin segments, 0.75.

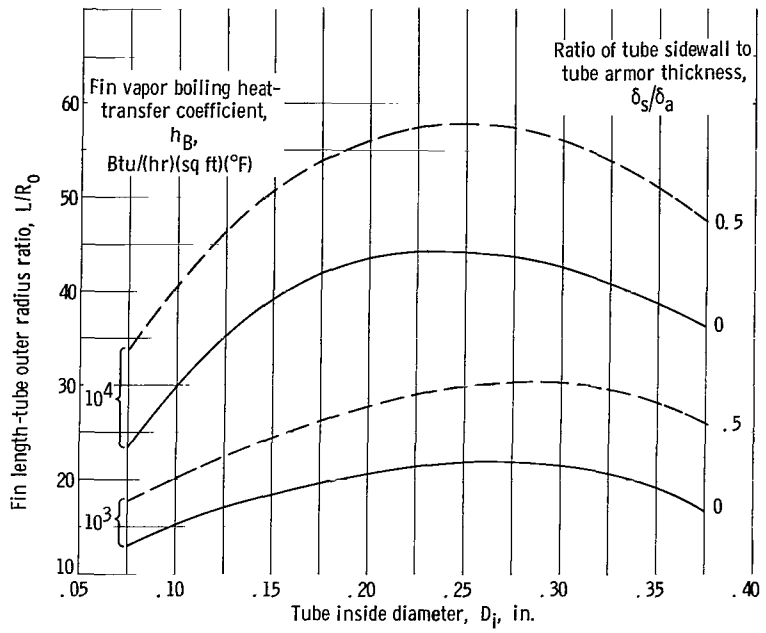

Figure 10. - Fin length-tube outer radius ratio L/R_o at peak heat rejection per unit weight for vapor-chamber fin-tube radiator. Fin segment planform area, 80 square inches; ratio of fin vapor boiling to fin vapor condensing heat-transfer coefficient, 1.0; tube-header nonpenetration probability, 0.90; ratio of surviving segments to total fin segments, 0.75.

Tube block armor thickness. - Variation of tube block armor thickness at peak heat rejection per unit weight with tube inside diameter is shown plotted in figure 9. The armor thickness decreases as the δ_s/δ_a ratio decreased for both values of h_B chosen. This is caused by a reduction in the vulnerable area of the tube block (function of R_b) with decreasing δ_s/δ_a. The armor thickness also decreases slightly with increasing tube inside diameter until a minimum is reached at a tube inside diameter of 0.20 to 0.25 inch. At this point the value of δ_a starts to increase once again.

The results show that a larger value of δ_a is obtained as the value of the boiling coefficient is decreased since at low values of h_B the ratio of fin area to tube area is decreased and thus results in an increased tube vulnerable area. The effect of varying N_s/N resulted in only a small variation in armor thickness for all the cases investigated. The magnitude of δ_a is small because of the low power level and low nonpenetration probability ($P(0)_t = 0.90$) considered for this analysis.

L/R_o ratio. - In figure 10, the L/R_o ratio for peak Q_{rej}/W is plotted against tube inside diameter for the vapor-chamber fin-tube geometry. Curves that are given for two values of h_B and two values of δ_s/δ_a indicate a sizable variation in L/R_o with tube diameter especially at high values of h_B. The large variation is due to large fin lengths and the relative flatness of the curves of figure 4 near maximum Q_{rej}/W. Increasing the value of δ_s/δ_a increases L/R_o regardless of the value of h_B chosen. The effect of decreasing the value of N_s/N from 0.75 to 0.5 resulted in a small re-

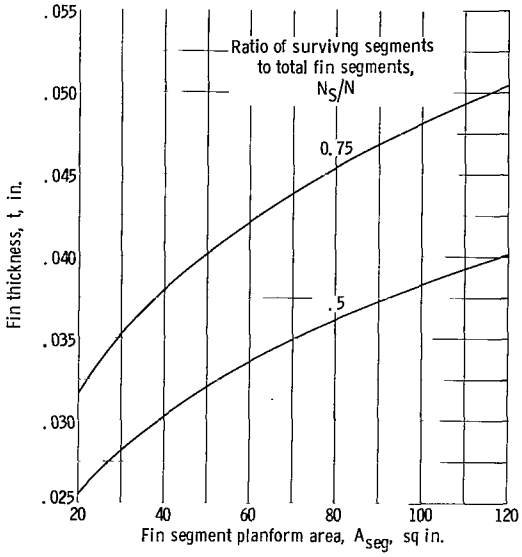

Figure 11. - Variation of fin thickness with fin segment planform area at maximum heat rejection per unit weight for vapor-chamber fin-tube radiator. Capillary weight, 0.1 pound per square foot; $h_B = h_C = 10^4$ Btu/(hr)(sq ft)(°F); probability of N_S or more segments not punctured, S, 0.90.

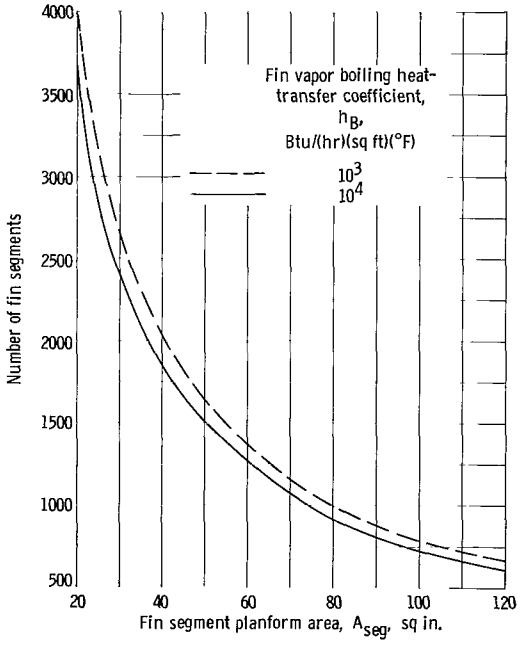

Figure 12. - Variation of number of fin segments with fin segment planform area at maximum heat rejection per unit weight. Capillary weight, 0.1 pounds per square foot; ratio of fin vapor boiling to fin vapor condensing heat-transfer coefficient, 1.0; tube-header nonpenetration probability, 0.90; ratio of surviving segments to total fin segments, 0.75; probability of N_S or more segments not punctured, S, 0.90.

duction in L/R_o. The magnitudes of L/R_o obtained at maximum heat rejection per unit weight were quite large compared to the results obtained for a high-temperature-level, high-power-level case presented in reference 9 where the values were approximately 2 to 4. Such high values of L/R_o are characteristic of low-temperature level radiators.

Fin thickness. - The vapor-chamber fin thickness is governed primarily by meteoroid protection considerations since heat transfer by conduction along the fin is not considered in the analysis (appendix C). The fin thickness at maximum Q_{rej}/W is plotted against fin segment planform area in figure 11 for two values of N_S/N. The increase in fin segment planform area, along with the necessary increase in the individual segment survival probability $P(0)_f$ for the same overall probability S, sharply increases the fin thickness. Increasing the value of N_S/N results in a larger fin thickness and thus in larger fin weight. Variations in boiling and condensing heat-transfer coefficients, tube block sidewall thickness ratio, and capillary weight resulted in a negligible change in fin wall thickness.

Number of fin segments. - The variation in the number of vapor-chamber fin segments with fin segment planform area is shown plotted in figure 12 for two values of boiling heat-transfer coefficient. The number of fin segments varies inversely with the fin segment planform area. Variations in tube diameter, in the ratio of the number of surviving segments to design segments, and in the tube block sidewall ratio, resulted in only small perturbations in the number of segments. The number of fin segments is quite large (600 to 4000), regardless of the choice of fin segment planform area considered. The large number of fin segments poses the fabrication problem

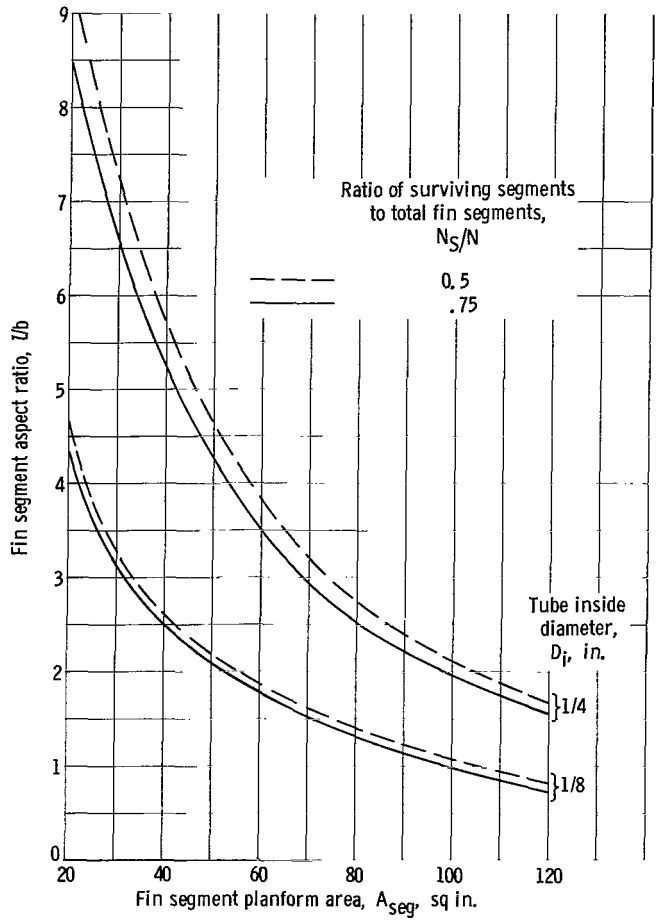

Figure 13. - Fin segment aspect ratio plotted against fin segment planform area for vapor-chamber fin-tube radiator. Capillary weight, 0.1 pound per square foot; $h_B = h_C = 10^4$ Btu/(hr)(sq ft)(°F); tube-header nonpenetration probability, 0.90; ratio of tube sidewall to tube armor thickness, 0.5.

of sealing each individual segment. Although it is desirable to operate at high values of A_{seg}, in order to reduce the number of segments, increased values of A_{seg} decrease the value of Q_{rej}/W (fig. 6, p. 10), and thus a compromise is required.

Another important consideration regarding the fin segment is its aspect ratio ℓ/b (fig. 3, p. 5), which for structural integrity should be in the neighborhood of 1 (square configuration). Figure 13 shows a plot of fin segment aspect ratio ℓ/b against fin segment planform area for two diameters that bracket the diameter at which maximum heat rejection per unit weight occurs. A value of $A_{seg} = 80$ square inches was chosen for the representative case and will be used for the radiator comparisons given later in the report. This value is a compromise between fin segment geometry and radiator weight.

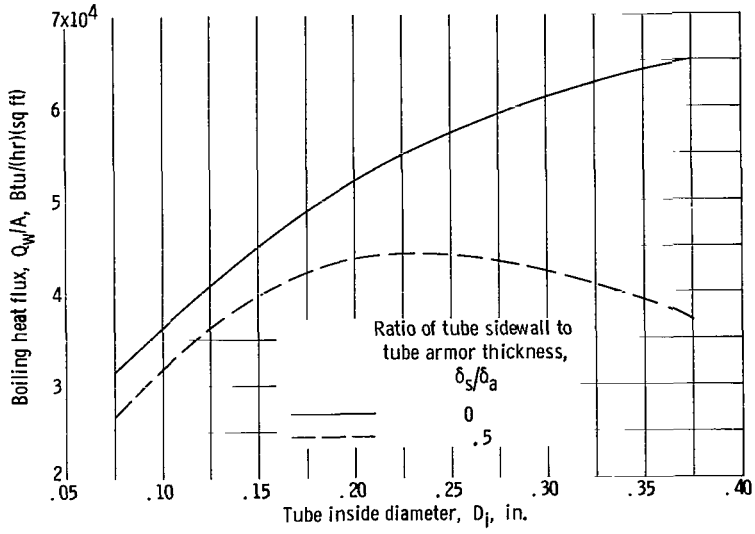

Figure 14. - Capillary fluid boiling heat flux for vapor-chamber fin-tube radiator. Fin segment planform area, 80 square inches; $h_B = h_C = 10^4$ Btu/(hr)(sq ft)(°F); ratio of surviving segments to total fin segments, 0.75.

Capillary Flow Requirements

The capillary fluid flow requirements for the vapor-chamber fin are determined by the heat flux at the boiling surface and the latent heat of vaporization of the capillary fluid chosen. The boiling heat flux is given by the expression

$$\frac{Q_w}{A} = \left(\frac{\ell}{R_o - t}\right)\sigma\epsilon T_f^4 \qquad (1)$$

The boiling heat flux obtained from the solutions of equation (1), which uses inputs obtained from the results of the radiator optimization, is plotted for peak Q_{rej}/W conditions in figure 14. The required heat flux is of the order of 5×10^4 Btu/(hr)(sq ft). The flux increases with increasing tube inside diameter for $\delta_s/\delta_a = 0.5$ up to a diameter of 1/4 inch, at which diameter the heat flux decreases. The heat flux for $\delta_s/\delta_a = 0$ continued to increase with increasing tube diameter. The reversal for the heat flux for $\delta_s/\delta_a = 0.5$ was brought about by a decreasing fin length at a diameter of 1/4 inch and larger. A decrease in heat flux with increasing sidewall thickness also occurred as shown in the figure. There was only a small variation in heat flux with N_s/N or with lower values of h_B.

Some low-temperature tests to date using water as the capillary fluid in fiber-glass wick material (ref. 10) yielded a heat flux range between 10^3 to 10^4 Btu/(hr)(sq ft). No other information has been found that would indicate what is required to achieve the higher needed heat fluxes.

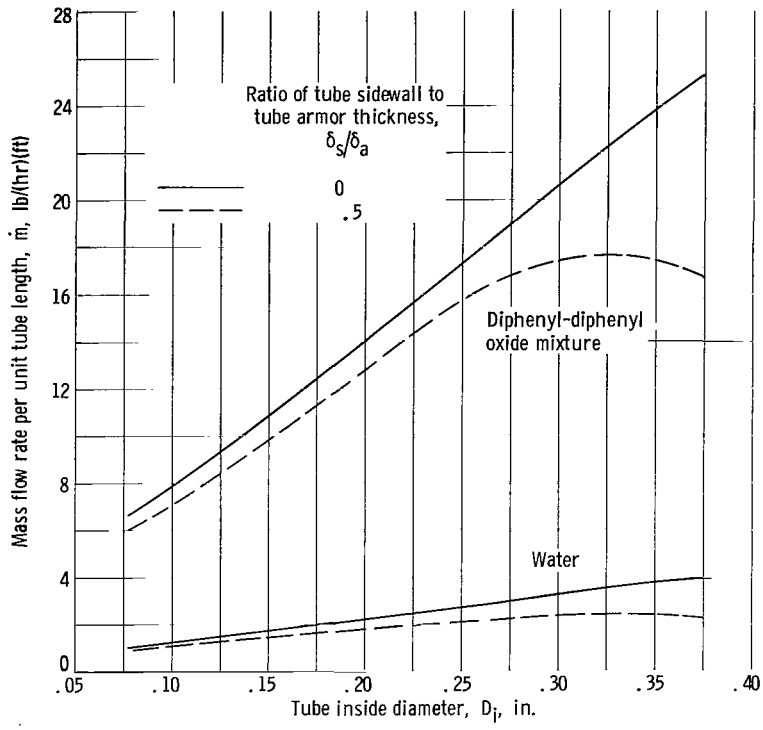

Figure 15. - Capillary fluid flow rate for vapor-chamber fin-tube radiator. Fin segment planform area, 80 square inches; $h_B = h_C = 10^4$ Btu/(hr)(sq ft)(°F); ratio of surviving segments to total fin segments, 0.75.

The mass flow rate of the capillary fluid is determined by the expression (ref. 9)

$$\dot{m} = \frac{2\epsilon \sigma \ell T_f^4}{h} \tag{2}$$

Results for equation (2) are plotted in figure 15 for peak Q_{rej}/W for two choices of capillary fluid. A diphenyl-diphenyl oxide mixture and water were chosen to illustrate the effect of latent heat of vaporization on the mass flow rate per unit length of tube. Water, which has the higher latent heat, had the lower mass flow rate of the two fluids. The temperature dependent vapor pressures of the two fluids selected, corresponding to boiling and condensing heat-transfer coefficients of 10^4 Btu/(hr)(sq ft)(°F), are approximately 2.86 and 195 psia for diphenyl-diphenyl oxide mixture and water, respectively.

Radiator Thermal Degradation

It was specified in the analysis of the vapor-chamber fin that 25 or 50 percent of the individual fin segments could be punctured by meteoroids. Upon puncture the chamber

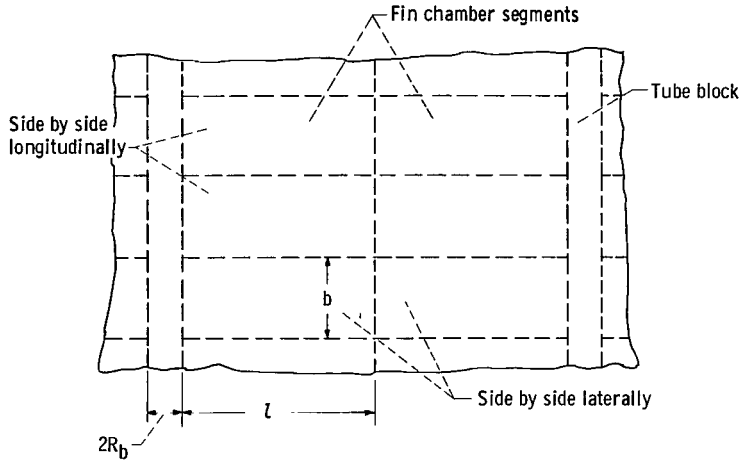

Figure 16. - Vapor-chamber punctured fin segment arrangement.

working fluid, which is under pressure, would be lost and the fin would no longer act as a vapor fin; however, the fin does not lose its radiating effectiveness entirely when punctured since it will then behave similarly to a solid-conducting double fin (fig. 2(b)). The degradation of the total heat rejection capabilities of the radiator with punctured fins then becomes a function of the number of surviving segments and the thermal effectiveness of the punctured fin segment.

The actual physical case would require a two-dimensional analysis, since the fin surfaces of the punctured segment can also receive heat by conduction axially from the fin surface of adjacent unpunctured segments and by radiation from the bulkheads of the segment. Thus the true radiating effectiveness of a single punctured fin would be greater than indicated for the one-dimensional situation of figure 2(b).

In the absence of a more complete two-dimensional solution, an initial simplified approach was used that considers each punctured fin segment as a double fin tube and uses the one-dimensional analysis of reference 8 to obtain the new fin thermal efficiency. The characteristic fin length used in obtaining the fin efficiency is designated to be the minimum fin dimension in the plane of the radiator. The characteristic fin length depends on the value of fin segment planform area, the segment aspect ratio ℓ/b, and the arrangement of the punctured segments, as shown in figure 16. For a single segment puncture, the characteristic fin length will be b or ℓ; for two segments punctured side by side laterally, the characteristic fin length will be b or 2ℓ; and for two segments punctured side by side longitudinally, the characteristic fin length will be ℓ or 2b.

The reduction in radiating effectiveness can be measured in terms of the ratio of the radiator heat rejection after vapor fin puncture to the design heat rejection with no fin puncture. The expression is

$$\eta_D = \frac{Q_{rej}(\text{after puncture})}{Q_{rej}(\text{design})} \tag{3}$$

The heat rejection after puncture is composed of the vapor header heat rejection $Q_{VH} = (1 - X_{tf})Q_{rej}$ which is not affected, the heat rejection from the vapor chamber fins and tubes not punctured $Q_{rej}X_{tf}(N_s/N)$, and the heat rejection of the fins and tubes that are punctured and assumed to act as a double fin-tube geometry according to

$$Q_D = 2\sigma\epsilon\ell\left(\eta_f + \frac{R_b}{\ell}\right)\left(1 - \frac{N_s}{N}\right)N_T Z T_b^4 \tag{4}$$

where the double fin thermal efficiency η_f is obtained by using the characteristic fin length associated with the punctured fin arrangement and the results of reference 8. It is assumed that the temperature of the adjacent hot chamber is maintained at the design value of T_f and, for simplicity of calculation, that the fin temperature is equal to the tube block sidewall temperature.

Figure 17 shows a plot of final one-dimensional thermal effectiveness ratio against fin segment planform area at peak Q_{rej}/W for the typical design condition chosen. The two tube diameters chosen bracket the range at which maximum heat rejection per unit weight occurs and indicate the possible variation in radiator thermal effectiveness depending on the choice of tube diameter. For the fin geometries involved in the calculations, only the b, ℓ, and 2b dimensions were required over the range of fin segment planform areas investigated.

In figure 17, for $D_i = 1/8$ inch and $N_s/N = 0.5$, the thermal effectiveness of the radiator follows the curve ABC as long as nonadjacent segments only are punctured. For segment areas up to 105 square inches (point B) the characteristic length is equal to b. Along the curve BC the characteristic length is ℓ. When two adjacent fins are punctured laterally, the thermal effectiveness follows the curve AB for small fin segment areas, but continues on the curve BD for larger areas as b remains the characteristic length. If the radiator is made up of adjacent pairs of longitudinally punctured segments, the thermal effectiveness follows the curve EF along which 2b is the characteristic length. At point F, 2b equals ℓ, and the thermal effectiveness follows the curve FC.

The curves for $N_s/N = 0.75$ (fig. 17(b)) follow the same pattern as those for $N_s/N = 0.50$ with the exception that the thermal effectiveness level is increased because of the larger fin thickness associated with the $N_s/N = 0.75$ case. The actual values of thermal effectiveness will occur between the single-puncture curve (A, B, C) and the double-puncture curve (E, F, C) depending on the frequency of single and double punctures.

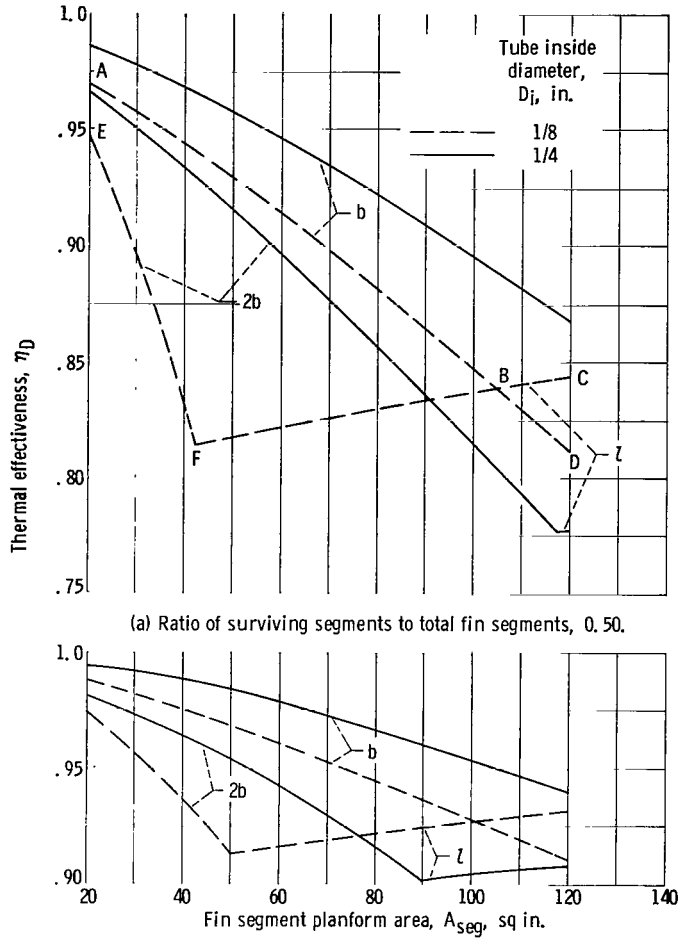

(a) Ratio of surviving segments to total fin segments, 0.50.

(b) Ratio of surviving segments to total fin segments, 0.75.

Figure 17. - One-dimensional vapor-chamber radiator thermal degradation. Capillary weight, 0.1 pound per square foot; $h_B = h_C = 10^4$ Btu/(hr)(sq ft)(°F); tube-header nonpenetration probability, 0.90; probability of N_S or more segments not punctured, S, 0.90.

COMPARISON OF RESULTS

The three fin-tube geometries, the vapor chamber fin-tube, and the solid-conducting central and double fin-tube radiators are compared in this section on the basis of weight, planform area, number of tubes, fin thickness, tube armor thickness, and panel aspect ratio. Because of the many variables involved in the vapor-chamber fin-tube radiator, a representative case was first selected for comparison with the other two geometries. Using the results presented in the previous section enabled the choice of $A_{seg} = 80$ square inches, which is based on a near square fin segment area, a boiling heat-transfer coefficient of 10^4 Btu/(hr)(sq ft) (^oF), a vapor chamber capillary medium weight of 0.10 pounds per square foot, and two values of N_s/N (0.5 and 0.75).

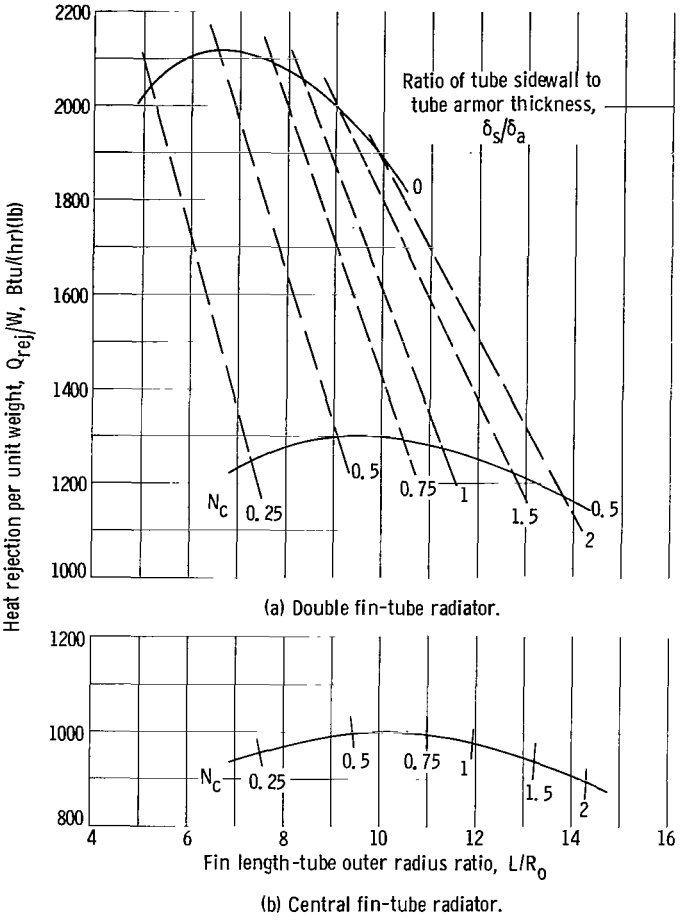

Figure 18. - Variations of heat rejection per unit weight with fin length-tube outer radius ratio L/R_o. Tube-header nonpenetration probability, 0.90; tube inside diameter, 0.125 inch.

Radiator Weight

Initially, the results of heat rejection per unit weight for the two solid-conducting fin-tube geometries were plotted against the L/R_o ratio for fixed values of the conductance parameters N_c (ref. 2). The largest value of heat rejection per unit weight for each constant N_c curve was then plotted against L/R_o as shown for the sample case of figure 18. The corresponding case of a sample plot of heat rejection per unit weight against L/R_o is shown for the vapor-chamber fin-tube geometry in figure 4.

A comparison of the peak heat rejection per unit weight results obtained from figures 4 and 18 along with results for additional tube inside diameters are shown in figure 19 for the three fin-tube geometries for two values of tube nonpenetration probability $P(0)_t$. Both the central and double fin-tube geometries reach maximum Q_{rej}/W at low diameters (0.10 to 0.15 in.) with Q_{rej}/W decreasing substantially as D_i increases. The tube block sidewall thickness ratio δ_s/δ_a has a small effect on the vapor fin radiator but a pronounced effect on the double fin radiator.

For $P(0)_t = 0.90$ (fig. 19(a)), at tube diameters corresponding to peak Q_{rej}/W for the solid-conducting fin radiators, the vapor-chamber fin geometry is clearly not superior to the other geometries in Q_{rej}/W. The vapor-chamber fin radiator, however, because of its small variation with diameter, becomes comparable to the double fin-tube radiator and somewhat better than the central fin-tube radiator at a diameter of 3/8 inch. At a value of $P(0)_t = 0.995$ (fig. 19(b)) the vapor chamber fin-tube radiator is considerably better than the central fin-tube radiator for all the diameters covered. Increases in Q_{rej}/W of from around 80 to 130 percent are indicated at maximum Q_{rej}/W. For $\delta_s/\delta_a = 0.5$, the vapor-chamber fin radiator is also substantially better than the double fin-tube radiator (order of 20 to 70 percent greater in maximum Q_{rej}/W). Only for $\delta_s/\delta_a = 0$ is the vapor-chamber fin-tube radiator not superior to the double fin-tube

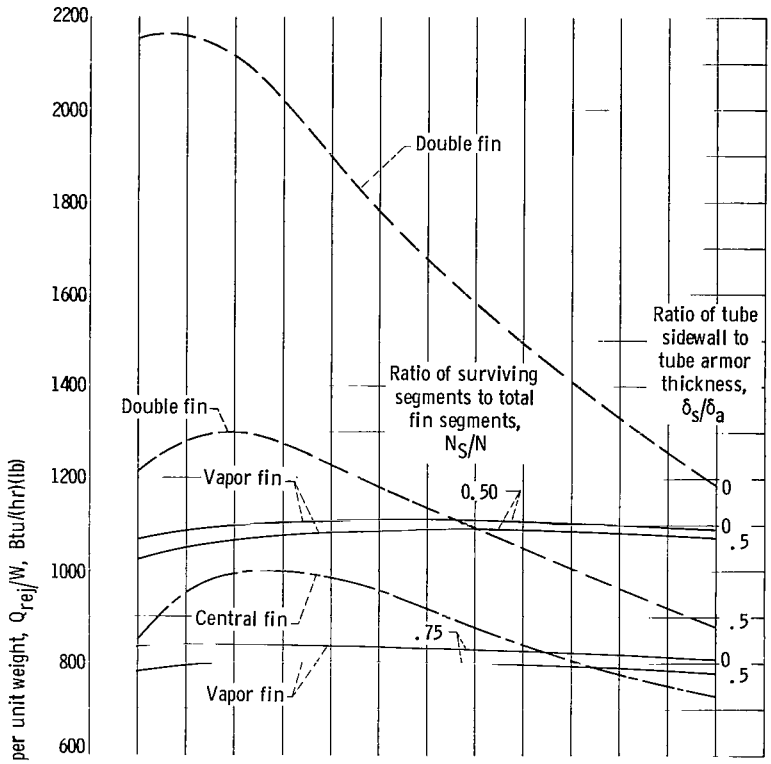

(a) Tube-header nonpenetration probability, 0.90.

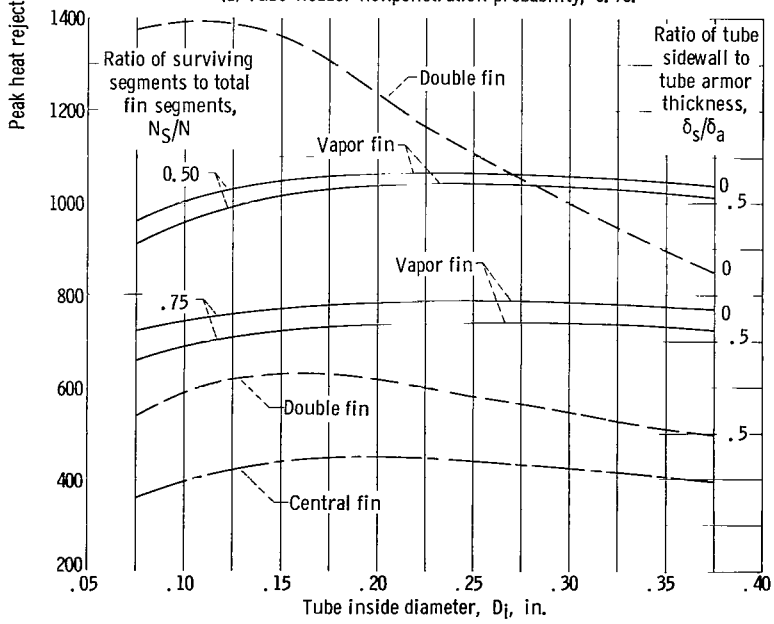

(b) Tube-header nonpenetration probability, 0.995.

Figure 19. - Comparison of peak heat rejection per unit weight. Fin segment planform area, 80 square inches; $h_B = h_C = 10^4$ Btu/(hr)(sq ft)(°F).

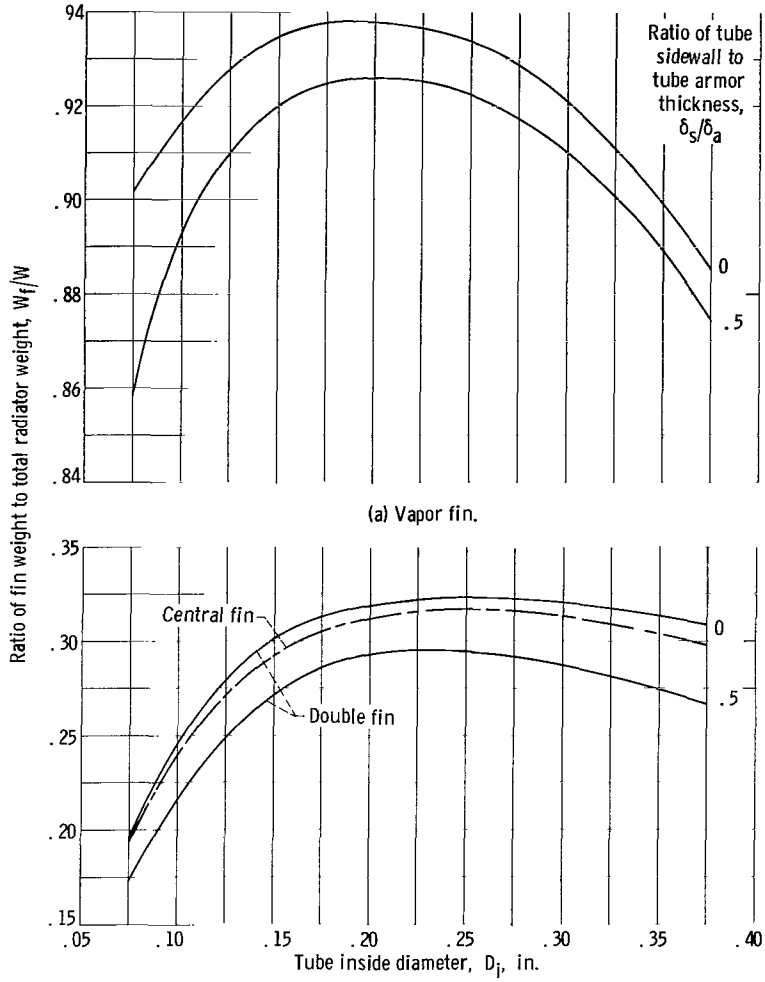

Figure 20. - Comparison of ratio of fin weight to total radiator weight at peak heat rejection per unit weight. Fin segment planform area, 80 square inches; $h_B = h_C = 10^4$ Btu/(hr)(sq ft)(°F); tube-header nonpenetration probability, 0.90; ratio of surviving segments to total fin segments, 0.50 and 0.75.

radiator at $P(0)_t = 0.995$.

The results of figure 19 are due to large differences in the proportion of the total weight involved in the fins of the solid-conducting and vapor-chamber fin-tube geometries as indicated in figure 20. The vapor-chamber fin-tube radiator has a large fin thickness, long fins, and thus more weight, whereas the double fin-tube geometry has small fin thickness, shorter fin length and thus less fin weight. This is brought about because the fin thickness for the vapor-chamber fin is determined by meteoroid puncture considerations as discussed in the CHARACTERISTICS section, and the double fin by heat-transfer optimization.

The effect of varying the tube and header nonpenetration probability $P(0)_t$ on maximum heat rejection per unit weight for the three fin-tube configurations is shown in

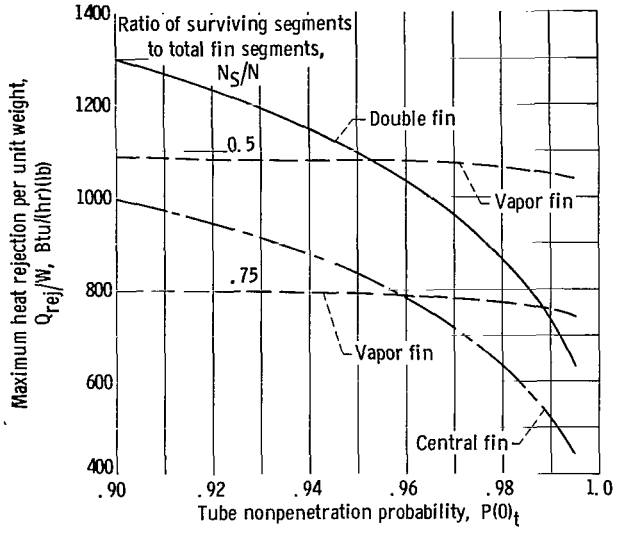

Figure 21. - Comparison of maximum heat rejection per unit weight plotted against radiator tube nonpenetration probability. Fin segment planform area, 80 square inches; capillary weight, 0.1 pound per square foot; $h_B = h_C = 10^4$ Btu/(hr)(sq ft)(°F); ratio of tube sidewall to tube armor thickness, 0.5; probability of N_S or more segments not punctured, S, 0.90.

figure 21 for $\delta_s/\delta_a = 0.5$. There is a sharp decrease in maximum Q_{rej}/W for the two solid-conducting fin-tube geometries as $P(0)_t$ increases but only a slight decline for the vapor-chamber fin radiator. Once again this is primarily due to the large proportion of the weight contained in the fins for the vapor-chamber fin-tube radiator. The relative weight comparison improves in favor of the vapor fin-tube radiator as the tube and header nonpenetration probability $P(0)_t$ is increased. For $N_S/N = 0.5$, the vapor fin becomes better than the double fin at $P(0)_t$ greater than 0.95. At $N_S/N = 0.75$ the double fin is always better than the vapor fin radiator. Thus, a more complete comparison between the geometries depends on a compromise between the weight and thermal degradation of the vapor-chamber fin radiator.

Radiator Geometry

Planform area. - Comparison of the planform area results of the three fin-tube geometries is shown plotted in figure 22. A sizable decrease in radiator planform area is afforded by the vapor-chamber fin-tube geometry compared with the other two fin-tube configurations over the entire range of tube inside diameters investigated. For the 30-kilowatt power level investigated, the vapor-chamber fin-tube geometry gives reductions in planform area of from 22 to 40 percent over the central fin-tube geometry for the full diameter range investigated. At the minimum weight condition, the planform area reduction is about 30 percent as shown in the figure. The vapor fin affords an approximately similar reduction in planform area compared to the double fin-tube geometry. Variations in δ_s/δ_a and N_s/N had little effect on radiator planform area.

The planform area of the vapor-chamber fin-tube geometry has a relatively flat variation with tube inside diameter and thus allows a wide choice of tube diameters (and correspondingly, of number of tubes) without compromising planform area or reducing radiator heat rejection per unit weight (fig. 19). The planform area of the

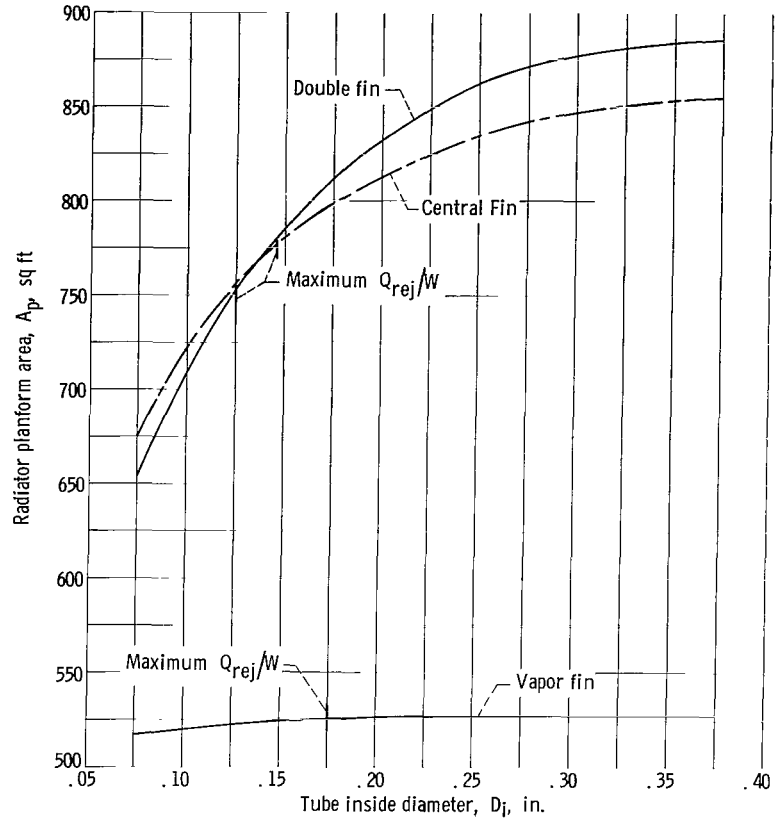

Figure 22. - Comparison of planform area at peak heat rejection per unit weight. Fin segment planform area, 80 square inches; $h_B = h_C = 10^4$ Btu/(hr)(sq ft)(°F); tube-header nonpenetration probability, 0.90; ratio of surviving segments to total fin segments, 0.75; ratio of tube sidewall to tube armor thickness, 0.5.

central fin and double fin geometries showed a substantial variation with tube inside diameter.

A concise way of showing the heat rejection per unit weight and radiator planform area comparisons at peak Q_{rej}/W for the three fin-tube geometries can be obtained by directly plotting Q_{rej}/W (from fig. 19(a)) and A_p (from fig. 22), as shown in figure 23 for $P(0)_t = 0.90$.

Number of tubes. - The number of radiator tubes for the three geometries at peak Q_{rej}/W was found to decrease substantially as the tube inside diameter increased, as shown in figure 24. In general, the vapor-chamber fin-tube geometry had the smallest number of tubes for any specific choice of tube inside diameter. Comparison of the number of tubes for the three radiators at the diameter corresponding to maximum heat rejection per unit weight (see fig. 19) indicated that the vapor-chamber fin-tube radiator at $\delta_s/\delta_a = 0.5$ required 13 tubes at a diameter of 1/4 inch, whereas the central fin-tube radiator had approximately 57 tubes at a diameter of 0.15 inch and the double fin-tube radiator had 85 tubes for $\delta_s/\delta_a = 0.5$ and a diameter of 0.125 inch. This trend also held for $\delta_s/\delta_a = 0$. An additional advantage of the vapor-chamber fin-tube radiator is

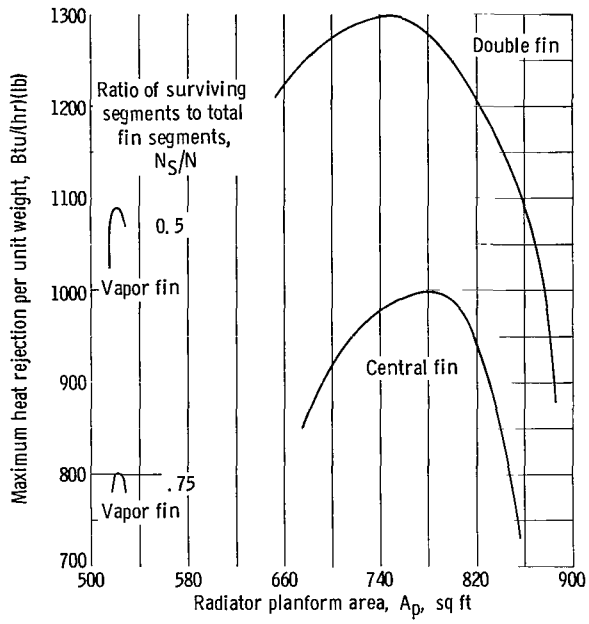

Figure 23. - Maximum heat rejection per unit weight plotted against radiator planform area. Fin segment planform area, 80 square inches; $h_B = h_C = 10^4$ Btu/(hr)(sq ft)(°F); tube-header nonpenetration probability, 0.90; ratio of tube sidewall to tube armor thickness, 0.5.

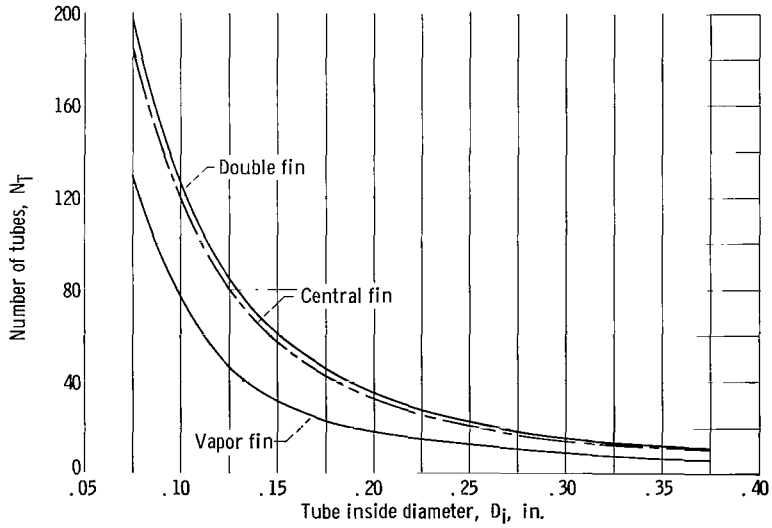

Figure 24. - Comparison of number of radiator tubes at peak heat rejection per unit weight at each diameter. Fin segment planform area, 80 square inches; $h_B = h_C = 10^4$ Btu/(hr)(sq ft)(°F); tube-header nonpenetration probability, 0.90; ratio of surviving segments to total fin segments, 0.75; ratio of tube sidewall to tube armor thickness, 0.5.

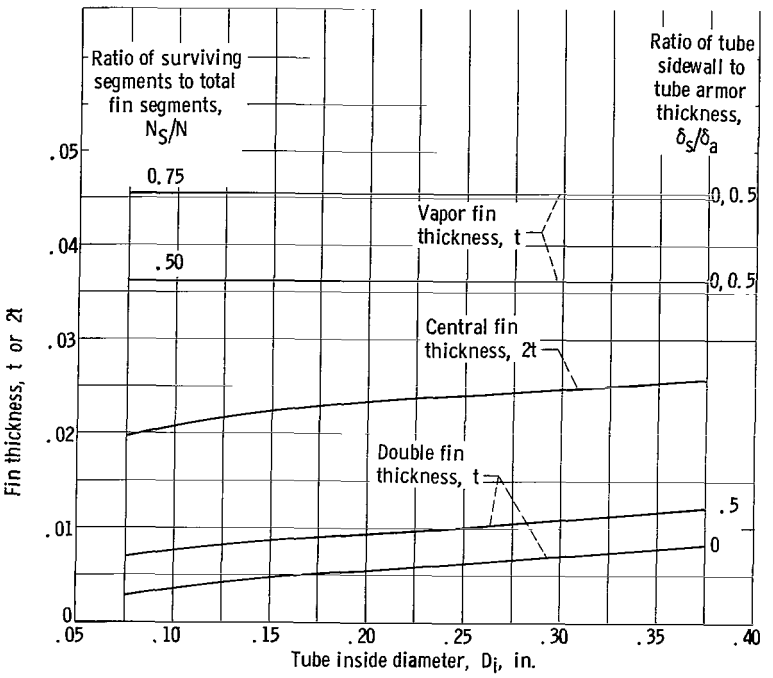

Figure 25. - Comparison of fin thickness at peak heat rejection per unit weight. Fin segment planform area, 80 square inches; $h_B = h_C = 10^4$ Btu/(hr)(sq ft)(°F); tube-header nonpenetration probability, 0.90.

that the number of tubes can be reduced even further by going to tube diameters larger than those required for minimum weight without a serious loss in Q_{rej}/W (fig. 19).

Fin thickness. - Comparison of the fin thickness obtained for the three fin-tube configurations is shown in figure 25. The fin thickness of the vapor-chamber radiator was constant with tube inner diameter, and the variation of t with δ_s/δ_a was negligible with capillary material weight or heat transfer coefficients. Because the vapor-chamber fin thickness is determined from meteoroid protection considerations, only such factors as A_{seg}, N_s/N, and S have an influence on its thickness. The thickness of the fin material of the vapor-chamber fin-tube radiator was considerably larger than that obtained for either of the solid-conducting fin configurations. The fin thickness 2t obtained for the central fin-tube radiator is approximately 0.025 inch, whereas the fin thickness t associated with the double fin-tube geometry is much less (from $t = 0.004$ at $\delta_s/\delta_a = 0$ to $t = 0.010$ at $\delta_s/\delta_a = 0.5$). Thus the minimum weight double fin-tube configuration for $\delta_s/\delta_a = 0$ may pose fabricational or structural problems.

The double fin-tube geometry, because of its high heat rejection per unit weight, may be worthwhile to explore since deviations from the maximum Q_{rej}/W conditions might improve fin thickness without a large sacrifice in weight. The fin thickness could be increased by varying the fin conductance parameter N_c, the L/R_o ratio, or the tube inside diameter D_i (discussed in a subsequent section).

L/R_o ratio. - The radiator fin-tube L/R_o ratio obtained for peak heat rejection

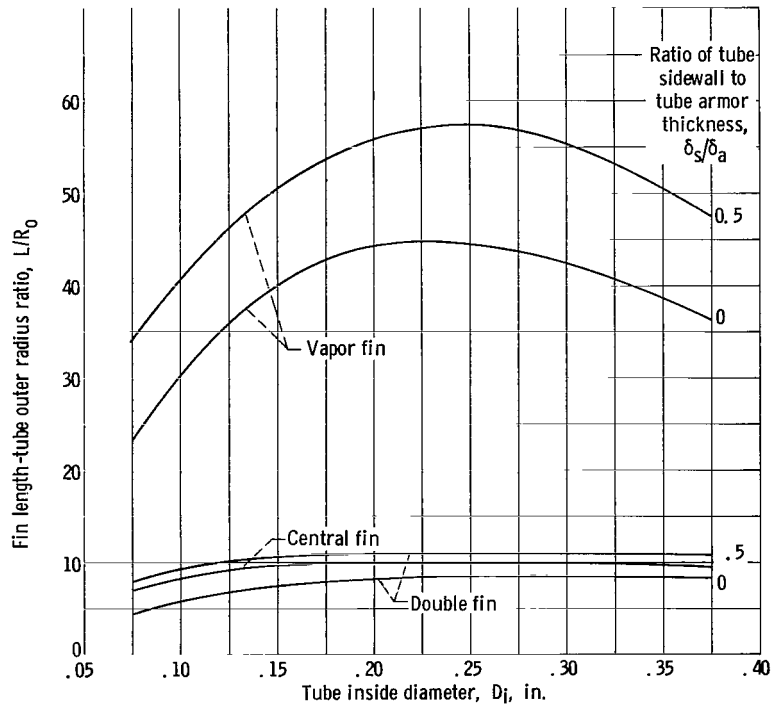

Figure 26. - Comparison of radiator fin length-tube outer radius ratio L/R_o at peak heat rejection per unit weight. Fin segment planform area, 80 square inches; $h_B = h_C = 10^4$ Btu/(hr)(sq ft)(°F); ratio of surviving segments to total fin segments, 0.75.

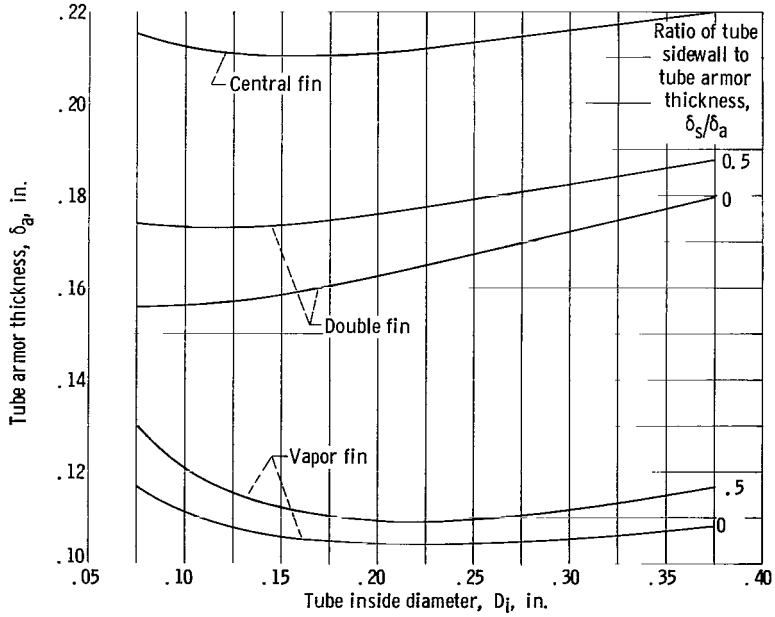

Figure 27. - Comparison of tube armor thickness at peak heat rejection per unit weight. Fin segment planform area, 80 square inches; $h_B = h_C = 10^4$ Btu/(hr)(sq ft)(°F); tube-header nonpenetration probability, 0.90; ratio of surviving segments to total fin segments, 0.75.

per unit weight at each diameter for the vapor-chamber, double, and central fin-tube geometries is shown plotted in figure 26. The L/R_o associated with the vapor chamber fin-tube geometry is much larger than that for the other two geometries (from 45 at $\delta_s/\delta_a = 0$ to 58 at $\delta_s/\delta_a = 0.5$) and peaks at a diameter of about 1/4 inch. The L/R_o ratio is seen to increase slightly for the double fin-tube geometries as the δ_s/δ_a ratio increases. Values of actual fin length ℓ for the vapor-chamber and double fin-tube radiators can be obtained from the value of L/R_o (fig. 26), the tube armor thickness (fig. 27), the ratio δ_s/δ_a, and equation (B6).

Tube armor thickness. - Figure 27 shows a plot of tube armor thickness δ_a against tube inside diameter for the three geometries investigated. Both the double and vapor fin radiators have less armor thickness than the central fin radiator since their vulnerable area is based on the projected area of the tube block rather than on the full outer surface of the tube, as in the case of the central fin radiator. Furthermore, the vulnerable area of the vapor fin is further reduced because of the smaller planform area resulting from the higher thermal effectiveness. The armor thickness for both the double and vapor-chamber fin-tube geometries decreases with decreasing δ_s/δ_a since the vulnerable area of the tube block decreases as the sidewall protection thickness δ_s decreases.

Panel aspect ratio. - Radiator panel aspect ratio w/Z is shown plotted for the three fin-tube geometries in figure 28 for the peak heat rejection per unit weight condition. A pronounced decrease in aspect ratio occurs with increasing tube diameter. In general, the vapor-chamber fin-tube geometry results in the largest aspect ratio. All three radiator configurations have aspect ratios less than 1.5 at tube diameters of practical interest (diameters greater than 1/8 in.). For the vapor fin and double fin radiators the effect of decreasing δ_s/δ_a from 0.5 to 0 resulted in a small decrease in aspect ratio. There was no appreciable change in w/Z with the value of N_s/N for the vapor-chamber fin-tube radiator.

Thermal Characteristics

Another interesting aspect that can be compared for the fin-tube geometries under investigation is the thermal characteristics of the fin for optimum radiator weight. Figure 29 shows a plot of the conductance parameter N_c at peak heat rejection per unit weight against tube inside diameter for the two solid-conducting fin-tube geometries. The conductance parameter for both the double and central fin-tube geometries increases with increasing tube inside diameter. This trend was also found to hold for the high-power-level investigation of reference 8. At the tube diameters that yielded minimum weight for the central and double fin configurations (0.125 in. $< D_i <$ 0.150 in.), the conductance parameter for both geometries was in the range 0.55 to 0.65 for the illustrative case presented.

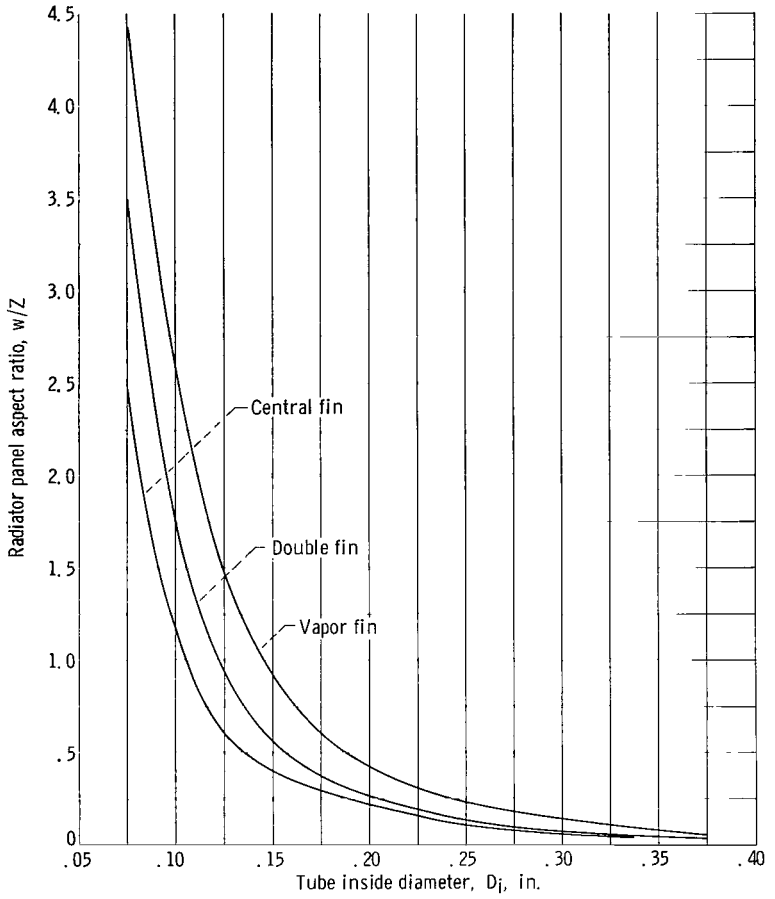

Figure 28. - Comparison of radiator panel aspect ratio at peak heat rejection per unit weight. Fin segment planform area, 80 square inches; $h_B = h_C = 10^4$ Btu/(hr)(sq ft)(°F); tube-header nonpenetration probability, 0.90; ratio of surviving segments to total fin segments, 0.75; ratio of tube sidewall to tube armor thickness, 0.5.

In many instances it is desirable to operate at fin-tube L/R_o ratios off the optimum value in order to compromise other radiator design conditions such as planform area or fin thickness. This can be accomplished for the two solid-conducting fin geometries by varying one or more of the following parameters: tube diameter, L/R_o, or conductance parameter. If for example, the tube diameter is assumed fixed at the value that yields minimum weight, the L/R_o ratio and N_c can be varied within a set allowable decrease in heat rejection per unit weight. A sample set of curves showing the zones of L/R_o and conductance parameters for near minimum weight is given in figure 30 for the central and double fin-tube radiators. The lowest N_c point on a curve corresponds to the minimum planform area of the radiator, whereas the maximum N_c point on a curve yields the maximum planform area.

In order to increase fin thickness for either the central or double fin-tube geometries, the fin should be designed to have a smaller value of conductance parameter N_c.

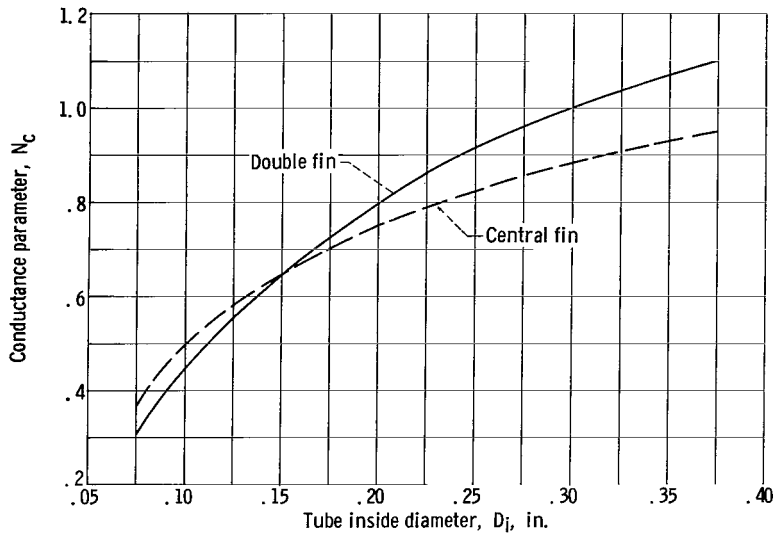

Figure 29. - Conductance parameter at peak heat rejection per unit weight. Tube-header nonpenetration probability, 0.90; ratio of tube sidewall to tube armor thickness, 0.5.

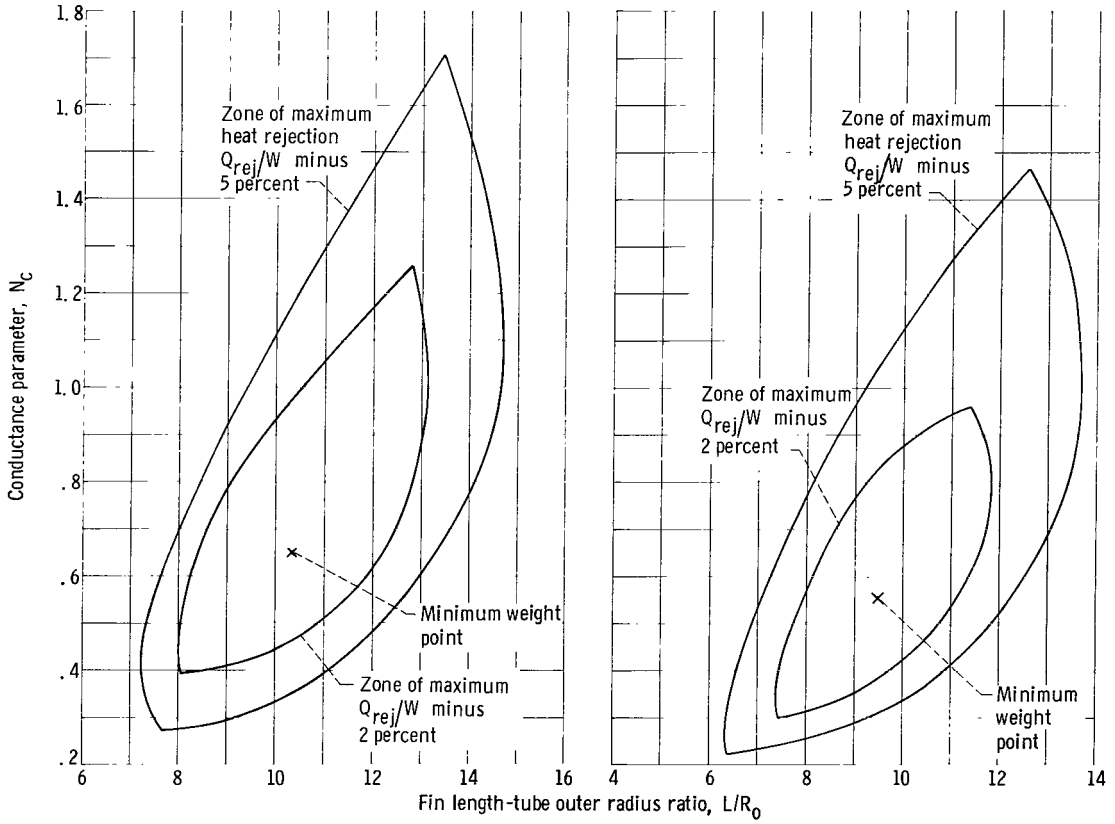

(a) Central fin-tube; tube inside diameter, 0.15 inch.

(b) Double fin-tube; ratio of tube sidewall to tube armor thickness, 0.5; tube inside diameter, 0.125 inch.

Figure 30. - Zones of fin length-tube outer radius ratio L/R_o and fin conductance parameters for near minimum weights. Tube-header nonpenetration probability, 0.90.

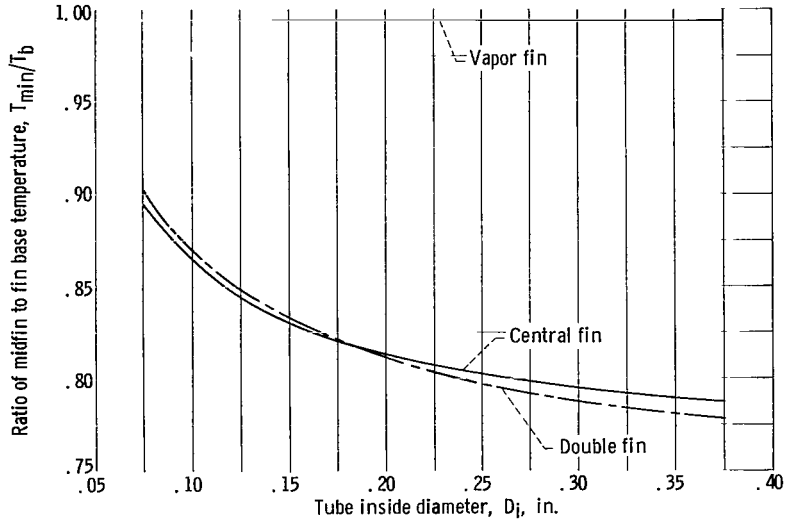

Figure 31. - Comparison of ratio of midfin to fin base temperature at peak heat rejection per unit weight. $h_B = h_C = 10^4$ Btu/(hr)(sq ft)(°F); tube-header nonpenetration probability, 0.90; ratio of surviving segments to total fin segments, 0.75; ratio of tube sidewall to tube armor thickness, 0.5.

Thus, for example, by reducing the conductance parameter N_c from 0.55 to 0.22 the fin thickness of a double fin-tube radiator can be increased from 0.008 to 0.015 inch with only a 5-percent penalty in heat rejection per unit weight (conditions of fig. 30(b)).

The thermal characteristics of the fin take on added importance when considering the resultant thermal stresses on a fin due to the inherent temperature drops in the solid conducting fin geometries. Typical results showing the ratio of mid-fin to fin-base temperature are shown plotted against tube inside diameter for the three fin-tube geometries in figure 31. The vapor fin exhibits a near isothermal gradient because of the internal mode of heat transfer and thus should pose no thermal stress problems during operation. If a vapor fin segment is punctured, a temperature drop less severe than that of the double fin would result, because the fin thickness is large compared to that of the double fin. Accordingly, the resultant thermal stress will be less than that exhibited by the double fin.

Comparison with High-Power-Level Results

The results and comparisons of the three fin-tube geometries obtained for this low-temperature-level, low-power-level study are a followup of a previous effort (ref. 9) which analyzed two high-power-level, high-temperature-level space radiator systems for a $P(0)_t = 0.995$ and $N_s/N = 0.75$. The results of reference 9 were for a columbium radiator for a 500-kilowatt power cycle and a beryllium radiator for a 1-megawatt power cycle, both of which had a radiator fluid inlet temperature of 1700° R. The comparisons

of the three fin-tube geometries for the high- and low-power-level cases will be made on the same basis: that is, at peak heat rejection per unit weight, at the same values of tube block sidewall ratio, vapor fin overall nonpenetration probability, tube and header nonpenetration probability, ratio of surviving to design fin segments, and for fin segment planform areas resulting in nearly square segments.

Radiator weight. - For the high-power-level radiators at $\delta_s/\delta_a = 0.5$, the vapor fin radiator with fin segment planform area equal to 20 square inches had a Q_{rej}/W from 50 to 68 percent greater than that for the double fin geometry, and from 60 to 87 percent greater than that for the central fin geometry. The low-temperature aluminum radiator for the 30-kilowatt power cycle at $\delta_s/\delta_a = 0.5$ and $A_{seg} = 80$ square inches indicated a reduced advantage (18 percent) for the vapor fin over the double fin geometry, and an advantage somewhat less than that for the high power level cases over the central fin-tube geometry (80 percent). Decreasing the tube block sidewall ratio from 0.5 to 0 gave the vapor fin geometry a decreased advantage in Q_{rej}/W over the double fin radiator of from 44 to 58 percent for the high power level cases but resulted in a sizable reduction in the value of Q_{rej}/W below that for the double fin geometry for the 30-kilowatt-power-level aluminum radiator.

The reduction in the Q_{rej}/W advantage of the vapor-chamber fin over the solid-conducting double and central fin geometries ($\delta_s/\delta_a = 0.5$) at the low power level is a result of the relative proportions of the total weight involved in the fins and in the tubes. At the low power level, the vapor chamber fins comprise 29 percent of the radiator weight, whereas at the two high power levels the fin weight is reduced to 13 to 15 percent of the total weight at a $\delta_s/\delta_a = 0.5$. Thus a reduction in the tube armor sidewall thickness will have a greater effect on the percent weight reduction for the high-power-level cases. The large fin weight for the low-power-level vapor-chamber case is brought about because of the large required planform area (similar in magnitude to the high-power-level radiators) in conjunction with the meteoroid puncture protection requirement of each individual fin chamber.

The double fin geometry is attractive on a weight basis for the 30-kilowatt case because of the high thermal conductivity of aluminum which allows long thin fins of relatively small weight. The lower thermal conductivity associated with the high-power-level beryllium and columbium radiators required relatively thicker fins and thus more weight for the solid-conducting fin geometries, which in turn gave an advantage to the vapor fin when compared on a weight basis.

Radiator geometry. - Other factors of interest in the high- and low-power-level radiator comparisons are geometric aspects such as radiator planform area which for the three fin-tube configurations investigated yields minimum area for the vapor-chamber fin-tube geometry for both power levels. In the low-temperature level case (fig. 22), a 20 to 40 percent decrease in planform area was obtained for the vapor-chamber fin-tube

geometry compared to either the central or double fin-tube configurations. For the high-temperature level, high-power-level case of reference 9, the planform area advantage of the vapor-chamber fin is reduced to between 18 to 32 percent for the columbium radiator and to between 12 and 21 percent for the beryllium radiator.

Comparison of the fin-tube configuration of the high- and low-temperature level solid-conducting fin cases indicated the low-temperature radiator resulted in values of L/R_o from three to five times larger than those characteristic of the high-temperature case. For the vapor-chamber fin-tube radiator, the value of L/R_o at low temperature was 8 to 12 times greater than the value at the high-temperature level. This large difference was brought about in part by the small tube inside diameters and armor protection thickness characteristic of low-temperature level, low-power-level systems and the large fin lengths required. Thin fins are another characteristic of the low-temperature solid-conducting double fin-tube configuration that may require an off optimum weight design in order to increase the thickness. At high-temperature level, the fin thickness is considerably larger and should not pose structural problems.

The large fin lengths at the low power level also indicated the need for longitudinal bulkheads for the vapor-chamber fins in order to improve the structural capability of the fin. The high-temperature, high-power case did not require the longitudinal bulkhead because of the relatively short fin lengths.

Thermal degradation. - Because of the high value of thermal conductivity for aluminum, the reduction in thermal effectiveness upon puncture of 25 percent of the fin segments is 4 to 6 percent less than that exhibited by the beryllium and columbium radiators, respectively. The relatively lower thermal degradation of the aluminum radiator can also allow operation at lower values of N_s/N, which tends to decrease the weight of the aluminum vapor fin radiator.

SUMMARY OF RESULTS

The analysis of the vapor-chamber fin-tube configuration for the 30-kilowatt low-temperature Rankine steam cycle yielded the following results:

1. The vapor-chamber fin-tube geometry at maximum heat rejection per unit weight is characterized by long fins (approx. 10 to 16 in.), tube inside diameters from 0.15 to 0.25 inch, and relatively few short tubes. Ratios of fin length to tube radius were on the order of 40 to 60.

2. Values of heat rejection per unit weight of the order of 600 to 1400 Btu/(hr)(lb) and planform areas of the order of 500 to 600 square feet were achievable for the vapor-chamber fin radiator for a zero degree sink temperature.

3. Relatively small variations with tube inside diameter were obtained for radiator

heat rejection per unit weight and radiator geometry (planform area, etc.) for the range of diameters from 0.075 to 0.375 inch at peak Q_{rej}/W conditions.

4. Because of the large amount of weight contained in the fins for the vapor-chamber fin-tube geometry, increasing the fin segment planform area (to reduce the number of fin segments) or the weight of the fin chamber capillary medium resulted in substantial reductions in heat rejection per unit weight.

5. Required capillary boiling heat fluxes were on the order of 5×10^4 Btu/(hr)(sq ft), while capillary fluid flow rates of 6 to 25 pounds per hour per foot of tube length were indicated for a diphenyl-diphenyl oxide mixture and approximately 1 to 4 pounds per hour per foot required for water.

6. A maximum thermal degradation of 20 percent was indicated for a 0.90 overall probability that 50 percent of the vapor-chamber fin segments would be punctured, while a maximum 10 percent degradation was indicated for a 75 percent survival.

7. Variation of the tube block sidewall thickness ratio had only a small effect on radiator weight and geometry for the vapor-chamber fin-tube.

A comparison of the vapor fin-tube geometry with the central and double fin-tube geometries indicated the following:

1. For a tube nonpuncture probability of 0.90, the vapor-chamber fin radiator was clearly not superior in heat rejection per unit weight to the central and double fin geometries. Largest values of heat rejection per unit weight were for the double-fin geometry radiator.

2. For a tube nonpuncture probability of 0.995, the vapor-chamber fin radiator had a substantially greater maximum heat rejection per unit weight compared to the central fin-tube radiator (80 to 130 percent increase) over the entire range of tube inner diameters from 0.075 to 0.375 inch. For $\delta_s/\delta_a = 0.5$, the vapor-chamber fin radiator was also substantially better than the double-fin radiator (order of 20 to 70 percent greater in maximum Q_{rej}/W). It was only for the case of $\delta_s/\delta_a = 0$ that the vapor-chamber fin radiator was not superior to the double fin radiator.

3. Radiator heat rejection per unit weight decreased substantially with increasing tube nonpenetration probability (from 0.90 to 0.995) for the central and double fin-tube geometries, whereas the vapor-chamber fin-tube geometry (with constant fin chamber nonpenetration probability) showed only a slight decrease.

4. The central and double fin-tube radiators reached peak heat rejection per unit weight at low tube inside diameters (0.10 to 0.15 in.) with the heat rejection per unit weight dropping off sharply with increasing tube inside diameter. The vapor-chamber fin-tube radiator reached its peak at larger diameters (0.15 to 0.25 in.) and exhibited relatively little variation with tube diameter.

5. A 20 to 40 percent reduction in radiator planform area is attained with the vapor-chamber fin-tube geometry over the central or double fin-tube radiators for peak

Q_{rej}/W conditions over the range of tube inner diameters considered.

6. In general, the vapor-chamber fin-tube radiator resulted in fin lengths two to four times greater than those of the central or double fin-tube radiators.

7. For all three radiator configurations considerable variation in panel aspect ratio could be obtained with only small weight penalties. For the two conducting fin geometries considerable latitude in fin thickness was also available for a small weight penalty.

Lewis Research Center,
National Aeronautics and Space Administration,
Cleveland, Ohio, July 15, 1965.

APPENDIX A

SYMBOLS

A	surface area, sq ft
A_p	radiator planform area, sq ft
A_{seg}	fin segment planform area, sq ft
A_v	vulnerable area for meteoroid protection, sq ft
b	fin segment width, ft
D	diameter, ft
D_i	tube inside diameter, ft
D_o	tube outside diameter, ft
E_a	Young's modulus of target material, lb/sq ft
F	view factor
g	conversion factor, ft lb_m/lb_f sec^2
h	heat of condensation, Btu/lb
h_B	fin vapor boiling heat-transfer coefficient, Btu/(hr)(sq ft)(^oF)
h_C	fin vapor condensing heat-transfer coefficient, Btu/(hr)(sq ft)(^oF)
J	mechanical equivalent of heat, 778(ft)(lb_f)/Btu
K_H	fluid pressure loss factor from header to tubes = 1.15
k	thermal conductivity, Btu/(ft)(hr)(^oF)
L	Minimum half length of fin between tubes, ($L^* - R_o$), ft
L^*	one half tube center to center distance, ft
ℓ	half length of fin between tubes, $L + \left(1 - \frac{\delta_s}{\delta_a}\right)\delta_a$, ft
$\dot{m}$	mass flow rate, lb/(hr)(ft)
N	number of fin segments
N_c	fin conductance parameter, $\frac{\sigma T_b^3 \ell^2}{kt}$
N_S	number of fin segments not punctured in given time τ
N_T	number of radiator tubes
P	cycle fluid pressure, psf
$P(0)$	probability of no critical damage to radiator tube, headers, or fin segments
Q_b	tube radiant heat rejection rate, Btu/hr
Q_D	heat rejection rate from punctured vapor fins and tubes, Btu/hr
Q_f	fin radiant heat rejection rate for a half fin length ℓ radiating from both sides, Btu/(hr)
Q_{rej}	total radiator heat rejection rate, Btu/hr
Q_{VH}	vapor header heat rejection rate, Btu/hr

q heat rejection rate per unit tube length, Btu/(hr)(ft)

R_b tube sidewall to tube centerline dimension,

$$R_b = R_o - \left(1 - \frac{\delta_s}{\delta_a}\right) \delta_a, \text{ ft}$$

R_i tube inside radius, ft

R_o tube outside radius, ft

S probability of N_s or more segments not punctured in time τ

T_S average vapor temperature in fin chamber, ^oR

T_b temperature of tube block outer surface, ^oR

T_f average temperature of fin surface, ^oR

T_w temperature of tube block sidewall, ^oR

T^* static fluid temperature at tube inlet, ^oR

t thickness of fin (double and vapor fin), half thickness of central fin, ft

u velocity of vapor, ft/sec

V velocity of liquid, ft/sec

W weight, lb

$\dot{W}$ mass flow per tube, lb/sec

w panel width, ft

X_{VH} fraction of total heat rejected by the vapor header

X_{tf} fraction of total heat rejected by the tubes and fins

Z tube length, ft

δ_a tube armor protection thickness, ft

δ_B fin longitudinal bulkhead thickness, ft

δ_c tube liner thickness, ft

δ_f fin transverse bulkhead thickness, ft

δ_s tube sidewall thickness, ft

ϵ surface hemispherical emissivity

η efficiency

η_D degraded radiator effectiveness

η^* effectiveness

θ temperature ratio, T/T_b

μ viscosity of working fluid, lb/(ft)(sec)

ρ density, lb/cu ft

$\overline{\rho_w \delta_w}$ capillary weight, lb/sq ft

σ Stefan-Boltzmann constant, 1.713×10^{-9} Btu/(sq ft)(hr)($^oR^4$)

λ vapor-chamber fin heat-transfer parameter

τ mission time, days

Subscripts

a tube armor

b tube base surface

c tube liner

f	fin
LH	liquid header
m	momentum
min	minimum
o	outside
p	particle
R	total
t	tube
VH	vapor header
w	tube block sidewall
0	conditions at tube inlet
3	radiator inlet conditions

APPENDIX B

HEAT-TRANSFER ANALYSIS

General Considerations

The heat rejection analysis involved considers the thermal characteristics of the central, double, and vapor fin-tube radiator configurations shown in figure 2. The governing equations that yield the fin temperature profiles for the three fin-tube configurations are developed in references 2, 8, and 9. Solution of these descriptive equations are then used to determine heat rejection characteristics, such as individual fin and tube thermal efficiency and total fin-tube thermal effectiveness. Basic equations describing the total fin-tube effectiveness for the central and double fin-tube geometries were derived by using blackbody considerations, whereas the vapor-chamber fin-tube geometry included the effect of emissivity. The blackbody heat rejection for the central fin was then multiplied by an apparent emissivity of the cavity formed by the tubes and fin (ref. 4). The blackbody heat rejection of the double fin-tube was multiplied by the surface emissivity because of the nature of the geometry.

In the analysis, it is assumed for the central fin and double fin geometries that energy input to the fin is composed of heat conduction along the fin from the fin base and incident radiation from the two base surfaces. In the case of the double fin tube configuration, additional incident radiation comes from the opposing fin surface. For the vapor fin-tube geometry the modes of heat flow in the fin consist of boiling a capillary fluid on the tube block sidewall and condensing it on the internal fin surface. The condensate on the fin surfaces is returned to the block surface by capillary pumping. Inasmuch as the fin and tube block temperature will not be very different, there will be only negligible additional heat input to the fin by conduction from the base and by radiation from the block surface. Radiant emission for the three geometries comes from both sides of the fin-tube panel to a surrounding environment of 0° R assumed for this comparison.

Several specific assumptions are used in the development of the fin-tube heat-transfer relation for all the geometries considered:

(1) Incident radiation from external sources is negligible.

(2) The effect of surface emissivities less than 1 on fin-tube thermal effectiveness is small and thus neglected.

(3) Steady-state one-dimensional heat flow occurs in the tube wall.

(4) The development of the fin and tube angle factors is based on an infinite longitudinal extent of fin and tube and zero fin thickness.

(5) The inside tube wall temperature is uniform circumferentially and equal to the static temperature of the fluid evaluated at the inlet conditions of the tube.

(6) Material properties such as thermal conductivity, modulus of elasticity, and emittance are constant and based on the tube inlet inside wall temperature.

Additional assumptions required for the vapor-chamber fin-tube configuration are

(1) Steady-state heat transport within the vapor chamber with uniform vapor saturation temperature along the length of the fin.

(2) The transverse and longitudinal bulkheads are adiabatic surfaces.

(3) The temperature of the fin surface and each tube block surface is uniform.

(4) Tube block outer wall and sidewall temperatures are equal (appendix C).

Central Fin-Tube (fig. 2(a))

The analysis of reference 13 was used to determine the fin temperature profile that in turn enabled the determination of the net heat rejected from the fin. The net heat loss Q_f from both sides of a fin of length L when compared to the ideal amount of energy that can be rejected from a black isothermal surface yields the following dimensionless expression for the thermal efficiency of the fin

$$\eta_f = \frac{\frac{Q_f}{Z}}{2\sigma L T_b^4} = -\frac{1}{N_c}\left(\frac{d\theta}{dX}\right)_{X=O} \tag{B1}$$

where $(d\theta/dX)_{X=0}$ is obtained from solutions for the fin temperature profile (ref. 13).

The base surface efficiency η_b is defined as the net heat loss from one-quarter of a tube outer surface Q_b divided by the maximum emission possible ($\epsilon = 1.0$) from the one-quarter periphery of the tube. The expression is

$$\eta_b = \frac{\frac{Q_b}{Z}}{\sigma \frac{\pi R_o}{2} T_b^4} = \frac{2}{\pi}\left[1 + \frac{L}{R_o}\int_0^1 (F_{X-1} + F_{X-2})(2 - \theta^4)dX\right] \tag{B2}$$

The integral in equation (B2) also makes use of the fin temperature profile (ref. 13).

The total thermal effectiveness of the fin and tube can then be obtained from the expression

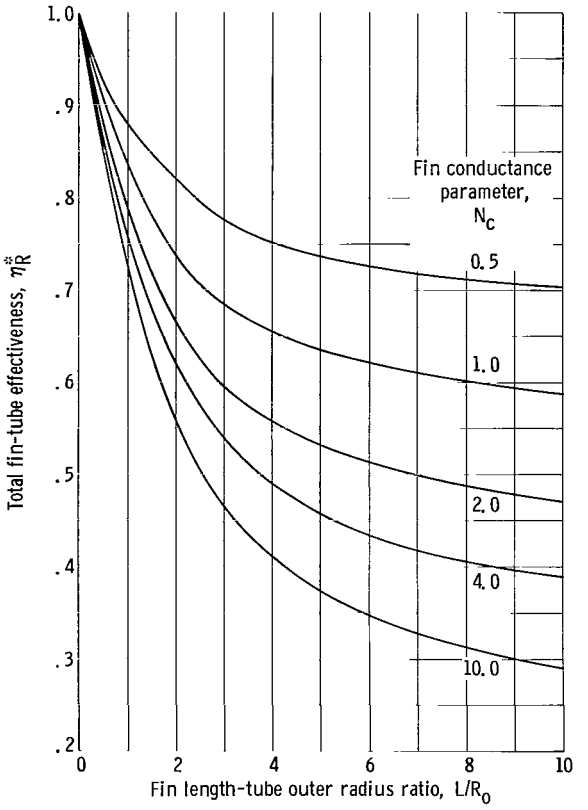

Figure 32. - Total fin-tube effectiveness plotted against fin length-tube outer radius ratio L/R_o for central fin-tube radiator.

$$\eta_R^* = \frac{\eta_f}{1 + \frac{R_o}{L}} + \frac{\frac{\pi}{2}\frac{R_o}{L}\eta_b}{1 + \frac{R_o}{L}} \qquad \text{(B3)}$$

The values of overall thermal effectiveness η_R^* obtained from equation (B3) are plotted against the fin profile ratio L/R_o for selected values of the conductance parameter N_c in figure 32.

The temperature drop in the tube wall $(T^* - T_b)$ is determined from one-dimensional conduction based on a heat flow from the inner to the outer wall which is rejected by radiation and is given by the expression (ref. 4)

$$\frac{\sigma\epsilon(D_i + 2\delta_c + 2\delta_a)}{2} T_b^4 \ln\left(\frac{D_i + 2\delta_c + 2\delta_a}{D_i + 2\delta_c}\right) - k(T^* - T_b) = 0 \qquad \text{(B4)}$$

Double Fin-Tube

The double fin-tube configuration shown in figure 2(b) used the analysis of reference 7 to obtain equations describing the radiant heat-transfer characteristics.

For this geometry the fin thermal effectiveness can be defined as the amount of energy rejected from the fin divided by the maximum that can be rejected from both sides of an isothermal black fin-tube geometry of length $2(\ell + R_b)$. This expression is

$$\eta_f^* = \frac{2\frac{Q_f}{Z}}{4\sigma\ell\left(1 + \frac{R_b}{\ell}\right)T_b^4} = \frac{1}{1 + \frac{R_b}{\ell}} \int_0^1 \theta^4 \, dX \qquad \text{(B5)}$$

The temperature profile θ (obtained from ref. 7) in equation (B5) is a function of position X on the fin for specific values of δ_s/δ_a, L/R_o, and N_c. The ratio R_b/ℓ in equation (B5) is defined in terms of δ_s/δ_a, which is the fraction of the armor thickness retained on the enclosed side of the tube block.

$$\frac{R_b}{\ell} = \frac{R_o - \left(1 - \frac{\delta_s}{\delta_a}\right)\delta_a}{L + \left(1 - \frac{\delta_s}{\delta_a}\right)\delta_a} \tag{B6}$$

The blackbody base-surface effectiveness can be calculated by the equation

$$\eta_b^* = \frac{2\frac{Q_b}{Z}}{4\sigma\ell T_b^4\left(1 + \frac{R_b}{\ell}\right)} = \frac{1}{\left(1 + \frac{\ell}{R_b}\right)} \tag{B7}$$

The total blackbody thermal effectiveness η_R^* is then obtained by adding the results of equations (B5) and (B7):

$$\eta_R^* = \frac{1}{\left(1 + \frac{\ell}{R_b}\right)}\left(1 + \frac{\ell}{R_b}\int_0^1 \theta^4\, dX\right) \tag{B8}$$

Solutions of equation (B8) are shown plotted in figure 33 against L/R_o for specific values of the conductance parameter N_c and δ_s/δ_a. The curves of figure 33 do not equal 1 at L/R_o equal to zero for δ_s/δ_a values other than 1 since a fin of length δ_s remains.

The temperature drop through the tube block (fig. 2(b)) is determined by using a simplified approach which assumes that the heat radiated from the exposed surface of the tube block is transferred from the tube inner surface across the length δ_a. The temperature drop equation is

$$\sigma\epsilon\delta_a T_b^4 - k(T^* - T_b) = 0 \tag{B9}$$

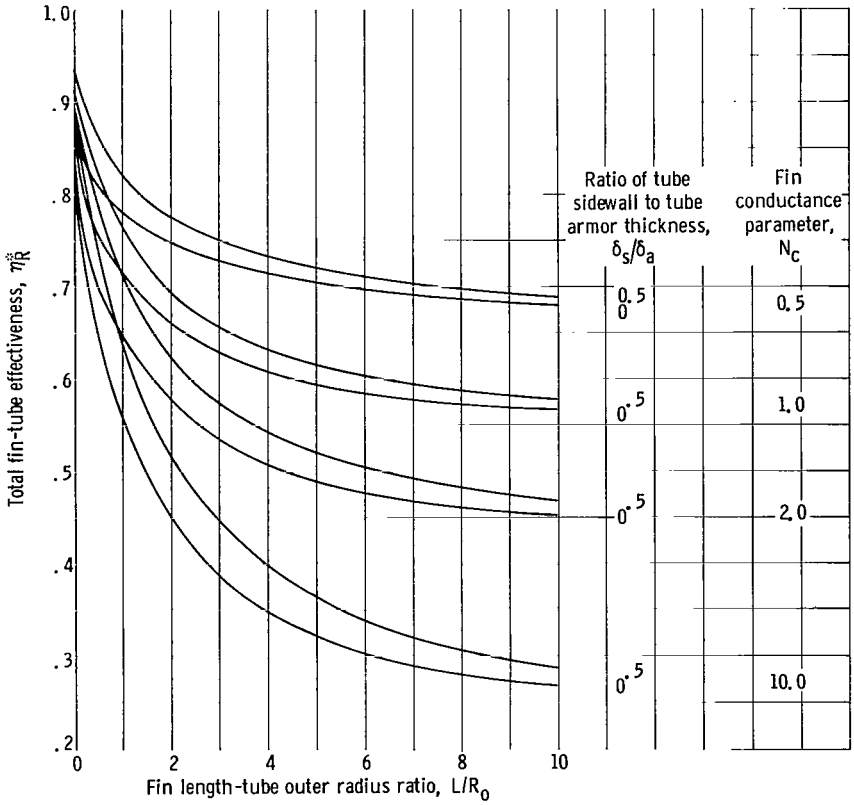

Figure 33. - Total fin-tube effectiveness plotted against fin length-tube outer radius ratio L/R_0 for double fin-tube radiator.

Vapor-Chamber Fin-Tube

Equations describing the internal heat-transfer mechanisms of the vapor-chamber fin along with an evaluation of the fin performance are given in appendix C. Using the results given in appendix C for the fin temperature profile (see eqs. (C4) and (C5)) enables the determination of the total fin-tube thermal effectiveness that can be obtained by comparing the tube block and fin net heat rejection with the maximum that can be rejected from a fin-tube of length $2(\ell + R_b)$:

$$\eta_R^* = \frac{2Q_f + Q_b}{4\sigma\epsilon\ell Z N_T \left(1 + \frac{R_b}{\ell}\right) T_b^4} = \frac{\left(\frac{T_f}{T_b}\right)^4 + \frac{R_b}{\ell}}{\left(1 + \frac{R_b}{\ell}\right)} \tag{B10}$$

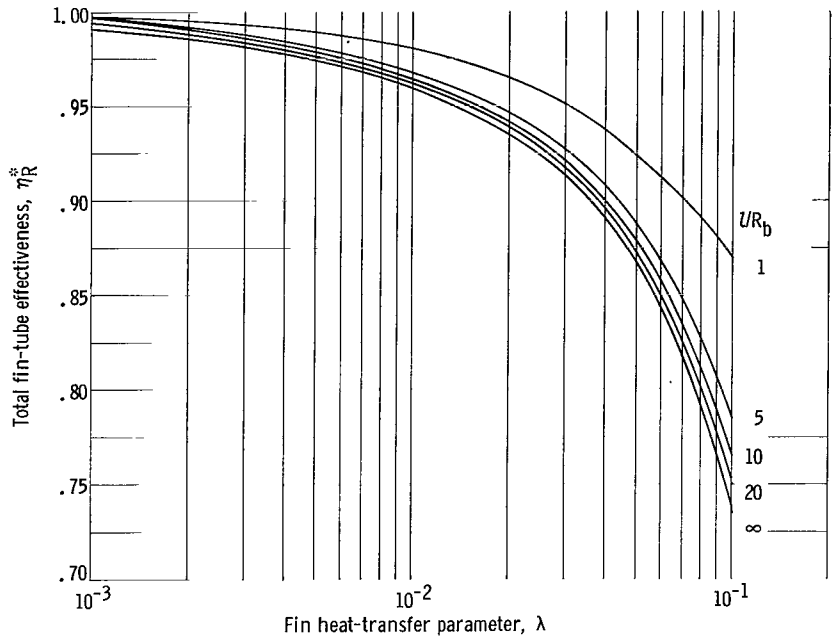

Figure 34. - Total fin-tube effectiveness for vapor-chamber fin-tube radiator.

The overall ratiating effectiveness is thus simply a function of the ratio of fin to block temperature T_f/T_b and the length ratio R_b/ℓ. The total fin-tube effectiveness can be written in terms of a dimensionless heat-transfer parameter λ by rewriting equation (C4), which yields the ratio T_f/T_b in the following form:

$$\frac{T_f}{T_b} + \lambda\left(\frac{T_f}{T_b}\right)^4 = 1 \tag{B11}$$

where the dimensionless fin heat-transfer parameter λ is

$$\lambda = \frac{\alpha\epsilon T_b^3}{h_B}\left(\frac{\ell}{R_o - t} + \frac{h_B}{h_C}\right) \tag{B12}$$

Figure 34 shows plots of η_R^* against λ for several values of ℓ/R_b. The curves of figure 34 show decreasing total effectiveness with increasing λ and ℓ/R_b.

APPENDIX C

VAPOR-CHAMBER FIN-TUBE THERMAL ANALYSIS

The thermal analysis of the vapor-chamber fin-tube configuration involves the determination of the tube block outer and inner wall temperature along with the average temperature of the fin surface. Factors affecting the thermal aspects of this configuration include heat-transfer coefficients for fin chamber boiling and condensing, materials, and chamber geometry. The analysis of this configuration is presented in detail in reference 9.

Tube Block Temperature

It was assumed earlier (appendix B) that the tube block sidewall temperature T_w was equal to the tube block outer surface temperature T_b in the determination of the thermal effectiveness of the vapor-chamber fin-tube. In order to check this assumption a detailed investigation is needed on the heat-transfer processes within the fin chamber and the tube block heat-transmission paths (fig. 2(c)). Equations describing the heat conduction through the tube walls, radiation from the outer surface to space, and the heat transferred by boiling to the capillary fluid are developed in detail in reference 9. This analysis yields the following relations describing the temperature ratio T_w/T_b:

$$\frac{T_w}{T_b} = 1 - \frac{\sigma\epsilon\delta_a T_b^3}{k}\left[\left(\frac{q_w}{q_b}\right)\left(\frac{\delta_s}{\delta_a}\right)\left(\frac{1 - \frac{\delta_s}{\delta_a}}{\frac{R_i}{\delta_a} + \frac{\delta_s}{\delta_a}}\right) - 1\right] \tag{C1}$$

The equation describing the outer surface temperature T_b is

$$T_b + \left(\frac{\sigma\epsilon\delta_a}{k}\right)T_b^4 = T^* \tag{C2}$$

The temperature T^* in equation (C2) is the tube inner surface temperature. This temperature is determined from the expression

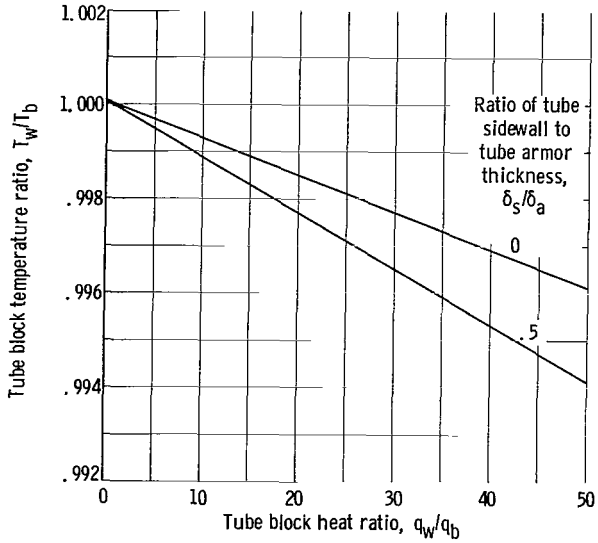

Figure 35. - Ratio of tube block sidewall to outer wall temperature ratio for vapor chamber fin-tube radiator. Static fluid inlet temperature, 836° R; fin segment planform area, 80 square inches; capillary weight, 0.10 pound per square foot; $h_B = h_C = 10^4$ Btu/(hr)(sq ft)(°F); tube inside diameter, 0.1 inch.

$$T^* = T_3 \left(1 - \frac{1}{2}\frac{K_H u_0^2}{Jgh}\right) \qquad (C3)$$

where T_3 is the stagnation temperature at the inlet to the radiator as obtained from the cycle calculations, u_0 is the tube inlet velocity, K_H is the header to tube pressure loss factor, and h is the vapor heat of condensation.

Equations (C1), (C2), and (C3) thus permit an evaluation of the ratio of the tube block outer surface temperatures T_w/T_b. Plots of T_w/T_b against the heat ratio q_w/q_b are presented in figure 35 for two values of δ_s/δ_a by using a set of geometry inputs and material constants typical of the examples considered herein. These results are for maximum heat rejection per unit weight conditions. Therefore, T_b and T_w can safely be assumed essentially equal for the class of examples treated herein.

Fin Temperature

The relation between the average fin temperature T_f and the tube block temperature T_b is given by the expression (ref. 9)

$$T_f + \frac{\sigma\epsilon}{h_B}\left(\frac{\ell}{R_o - t} + \frac{h_B}{h_C}\right)T_f^4 = T_b \qquad (C4)$$

and

$$T_f^4 = \frac{k(R_o - t)}{\delta_a \sigma\epsilon\ell\left(\frac{\delta_s}{\delta_a}\right)}(T^* - T_b) \qquad (C5)$$

where the above two relations are a result of heat balances on the fin chamber. Thus, the simultaneous solution of equations (C4) and (C5), along with the value of δ_a ob-

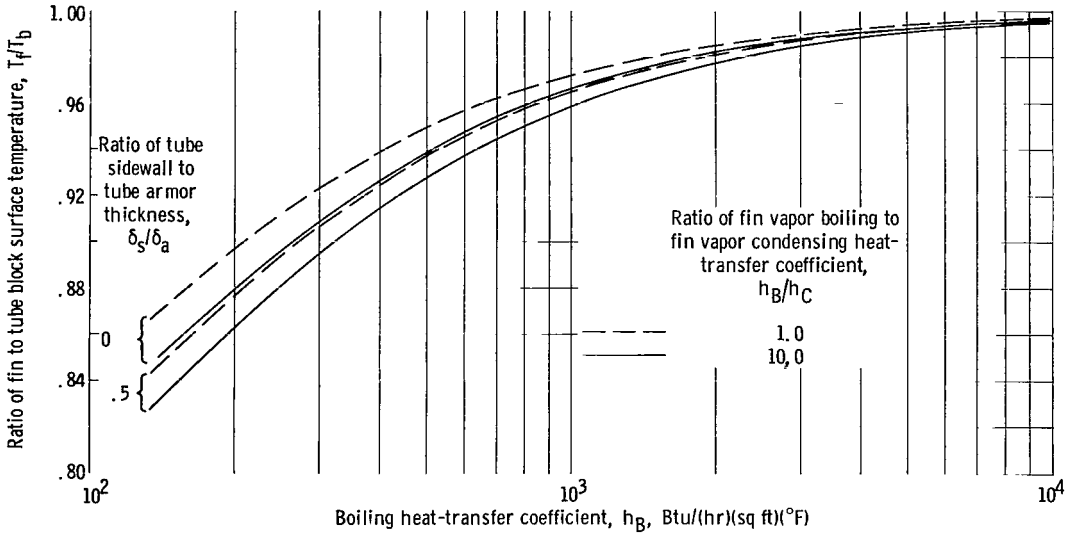

Figure 36. - Variation of ratio of fin to block surface temperature with boiling heat-transfer coefficient for vapor-chamber fin-tube radiator. Fin segment planform area, 80 square inches; capillary weight, 0.1 pound per square foot; tube-header nonpenetration probability, 0.90.

tained from figure 9, yields the fin temperature T_f and the tube block surface temperature T_b as a function of T^*, which enables the formation of the ratio T_f/T_b. When δ_s/δ_a equals zero, T^* equals T_b and only equation (C4) is required for the determination of T_f and the ratio T_f/T_b. This ratio is plotted as a function of the boiling heat-transfer coefficient h_B for the typical example condition in figure 36. For the boiling and condensing coefficient ratios considered (1.0 and 10) fairly low values of the boiling heat-transfer coefficient (order of 650 to 1000, depending on the choice of δ_s/δ_a) are adequate to maintain the fin-tube block temperature ratio above 0.96.

APPENDIX D

RADIATOR WEIGHT AND GEOMETRY

The equations and methods used in describing the weight and geometry of the central, double, and vapor-chamber fin-tube radiators are the same as those used in references 4, 8, and 9, respectively.

Radiator Weight

The total weight of the radiator is comprised of the individual weights of the vapor header, liquid header, tube block, and fin chamber:

$$W = W_{VH} + W_{LH} + W_{t,f} \tag{D1}$$

The tube and fin weight $W_{t,f}$ in the above equation can be calculated by summing the individual weights of the tube liner, armor, and fins. For the fin and tube geometries considered in this comparison, the weights are as follows:

Central fin and tube. -

$$W_{t,f} = N_T Z \left\{ \frac{4\rho_f \sigma R_o^3 T_b^3}{kN_c} \left(\frac{L}{R_o}\right)^3 + \pi \left[\rho_c \delta_c (D_i + \delta_c) + \rho_a \delta_a (D_i + 2\delta_c + \delta_a)\right] \right\} \tag{D2}$$

Double fin and tube. -

$$W_{t,f} = \frac{4\rho_f N_T Z \sigma T_b^3}{kN_c} \left[\frac{L}{R_o} + \left(1 - \frac{\delta_s}{\delta_a}\right)\frac{\delta_a}{R_o}\right]^3 (R_i + \delta_c + \delta_a)^3 + \rho_c \pi \delta_c N_T Z (D_i + \delta_c)$$

$$+ \rho_a N_T Z \left\{ 2(D_i + 2\delta_c + 2\delta_a) \left[R_i + \delta_c + \left(\frac{\delta_s}{\delta_a}\right)\delta_a\right] - \pi (R_i + \delta_c)^2 \right\} \tag{D3}$$

Vapor-chamber fin and tube. -

$$W_{t,f} = \rho_a N_T Z\left[4R_o R_b - \pi(R_i + \delta_c)^2\right] + \rho_c \pi N_T Z \delta_c (D_i + \delta_c) + 4N_T Z\left[\ell(\rho_f t + \overline{\rho_w \delta_w}) + (R_o - t)\overline{\rho_w \delta_w}\right] + 4\rho_f \delta_f \ell (R_o - t)(N + N_T) + 2\rho_f \delta_B (R_o - t) N_T Z \quad \text{(D4)}$$

The tube block armor thickness δ_a was determined by using the meteoroid protection criteria given in reference 11. The armor thickness δ_a was obtained from the equation (ref. 9)

$$\delta_a = \frac{1.48}{\rho_a^{1/6} E_a^{1/3}} \left(\frac{A_v \tau}{-\ln P(0)_t}\right)^{0.249} \quad \text{(D5)}$$

The total exposed area to be protected by direct impacts A_v is assumed to be the sum of the outer surface of the vapor header, twice the projected area of the tube block for the double and vapor fin-tube geometries, or the outer surface area of the round tube in the case of the central fin-tube geometry. The surface area of the liquid header, being relatively small, was neglected. For the central fin-tube the expression for the total vulnerable area is

$$A_v = \frac{Q_{rej}}{\sigma \epsilon}\left[\frac{1 - X_{VH}}{\frac{2}{\pi}\left(1 + \frac{L}{R_o}\right)\eta_R^* T_b^4} + \frac{X_{VH}}{F_{VH} T_3^4}\right] \quad \text{(D6)}$$

and for the double and vapor fin-tube the expression is

$$A_v = \frac{Q_{rej}}{\sigma \epsilon}\left[\frac{1 - X_{VH}}{\left(1 + \frac{\ell}{R_b}\right)\eta_R^* T_b^4} + \frac{X_{VH}}{F_{VH} T_3^4}\right] \quad \text{(D7)}$$

where T_b is a function of T_3 in the above two equations and is obtained from equations (B4), (B9), and (C2) for the central, double, and vapor-chamber fin-tube geometries, respectively, and equation (C3). The overall fin-tube effectiveness η_R^* is obtained from the results of equations (B3), (B8), and (B10), respectively, for the three geometries.

In equation (D3) the number of fin segments N is obtained from the expression

$$N = \frac{Q_{rej}(1 - X_{VH})}{2A_{seg}\epsilon\sigma\left(1 + \frac{R_b}{\ell}\right)\eta_R^* T_b^4} \tag{D8}$$

The fin thickness for the vapor-chamber fin in equation (D3) is determined by using meteoroid protection criteria similar to that used for the vapor fin radiator in reference 9. This equation is

$$t = \frac{1.48}{\rho_a^{1/6} E_a^{1/3}} \left[\frac{2A_{seg}\tau}{-\ln P(0)_f}\right]^{0.249} \tag{D9}$$

where A_{seg} is the fin chamber planform area (based on a fin length of ℓ) and $P(0)_f$ is obtained from figure 37 after N is known (ref. 14).

The value of δ_a computed for the tube armor was also applied as meteoroid protection on the vapor and liquid headers. The equations describing the weights of the vapor and liquid headers are the same as those developed in reference 4. The vapor header weight is given by

$$W_{VH} = \frac{4\pi w}{3}\left[(D_{VH} + \delta_{VH,c})\delta_{VH,c}\rho_c + (D_{VH} + 2\delta_{VH,c} + \delta_a)\delta_a\rho_a\right] \tag{D10}$$

and that of the liquid header and condensate by

$$W_{LH} = 4\pi w\left[\frac{\rho_\ell D_{LH}^2}{4} + \rho_c\delta_{LH,c}(D_{LH} + \delta_{LH,c}) + \rho_a\delta_a(D_{LH} + 2\delta_{LH,c} + \delta_a)\right] \tag{D11}$$

Once the weights for the three geometries were determined the total heat rejection per unit weight was expressed as

$$\frac{Q_{rej}}{W} = \frac{\frac{Q_{rej}}{N_T Z}}{\frac{W}{N_T Z}} \tag{D12}$$

The total heat rejection Q_{rej} is composed of the amount radiated from both sides of the fin-tube panel and that radiated from the vapor header. This heat rejection when

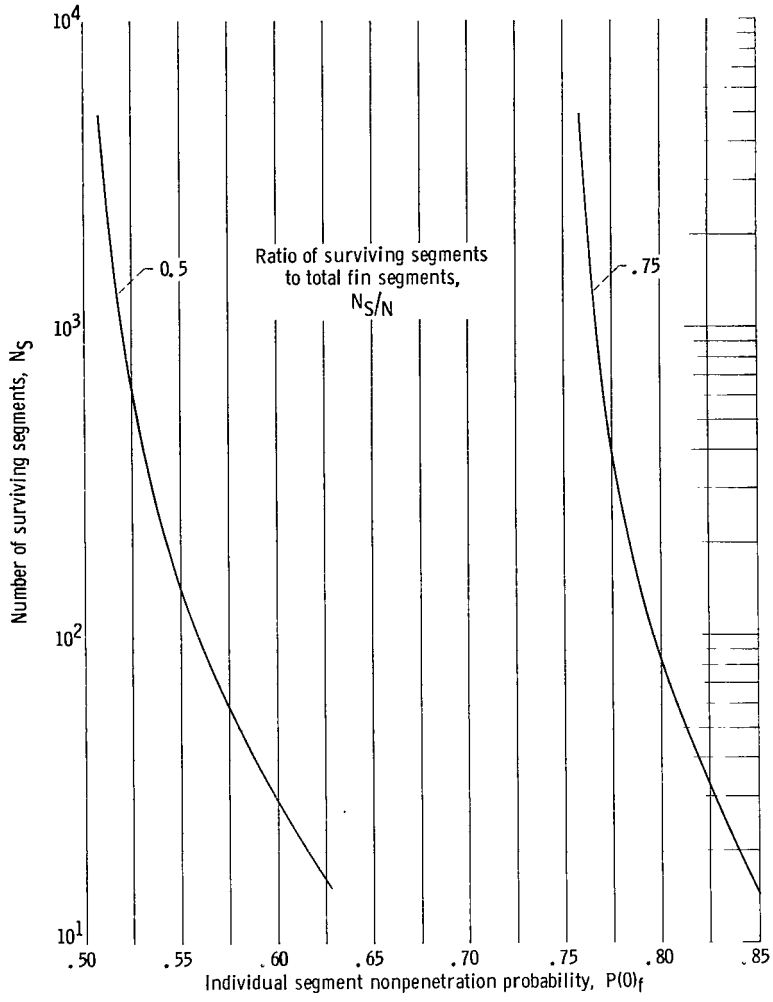

Figure 37. - Nonpenetration probability of one segment of segmented vapor-chamber fin-tube radiator. Probability of N_S or more segments not punctured, S, 0.90.

divided by the total tube length yields the expression

$$\frac{Q_{rej}}{N_T Z} = \sigma \epsilon R_b \left(1 + \frac{\ell}{R_b}\right)\left(4\eta_R^* T_b^4 + 1.045 \frac{D_{VH} F_{VH} T_3^4}{Z}\right) \tag{D13}$$

The denominator of equation (D12) can be found by dividing the total radiator weight (eq. (D1)) by the total tube length $N_T Z$ obtained from the results of the pressure drop analysis (appendix E) and the radiator optimization procedure. The peak value of Q_{rej}/W can then be obtained by plotting the results of equation (D12) as a function of the variables of interest.

Radiator Geometry

Radiator planform area A_p is obtained from the equation

$$A_p = \frac{Q_{rej}(1 - X_{VH})}{2\sigma\epsilon T_b^4 \eta_R^*} \tag{D14}$$

It is seen from the above equation that planform area will vary inversely with overall fin-tube effectiveness η_R^* for a specific choice of power and temperature level. The planform area will generally increase with increasing ℓ/R_b because η_R^* decreases as ℓ/R_b is increased (figs. 32, 33, and 34).

Another important factor with respect to the geometry of the three fin-tube configurations is the magnitude of the fin thickness. Fin thickness is determined for the central and double fin-tube geometries from the results of the fin heat rejection and weight optimization, whereas the fin thickness for the vapor-chamber fin is determined herein from meteoroid protection considerations according to equation (D9). The thickness of the vapor-chamber fin wall, however, should also be substantial enough to withstand anticipated pressure.

Additional radiator geometry such as panel aspect ratio (ratio of panel width w to tube length Z), number of tubes, and tube armor thickness are determined from the results of the optimization procedure.

APPENDIX E

PRESSURE DROP

Another factor that is required to determine the geometry and weight of a radiator is the allowable pressure drop in the radiator tubes and headers. This aspect of radiator design helps determine the vapor header geometry and the required tube diameter, tube length, and the number of tubes. The total pressure drop in the radiator is made up of ΔP in the vapor header, tube entrance turning loss, ΔP in the tubes, and ΔP in the liquid header. The total pressure drop, which is an input, is divided by the header inlet pressure P_3 and thus defined as

$$\left(\frac{\Delta P}{P_3}\right)_{total} = \left(\frac{\Delta P}{P_3}\right)_{VH} + \left(\frac{\Delta P}{P_3}\right)_{entrance} + \left(\frac{\Delta P}{P_3}\right)_{tubes} + \left(\frac{\Delta P}{P_3}\right)_{LH} \tag{E1}$$

The treatment of the pressure drop in the vapor header, the loss at the tube entrance, and the two-phase friction pressure drop and momentum pressure rise in the tubes is given in detail in reference 4.

The pressure drop in the liquid header is specified as a fraction of the pressure at the inlet of the vapor header $(\Delta P/P_3)_{LH}$. The diameter of the liquid header is obtained by applying Fanning's equation with a friction factor for turbulent flow. Also, noting that the liquid header is not tapered and that the liquid velocity increases uniformly from zero at one end to a maximum value at the header outlet yield the following equation for the liquid header diameter:

$$D_{LH} = \left[\frac{0.000065w(\mu_{\ell})^{0.2}\dot{W}^{1.8}}{\rho_{\ell}P_3\left(\frac{\Delta P}{P_3}\right)_{LH}}\right]^{0.2083} \tag{E2}$$

The maximum velocity in the liquid header can then be obtained by applying the continuity equation to the flow at the header outlet:

$$V_{LH} = \frac{\dot{W}}{\pi\rho_{\ell}D_{LH}^2} \tag{E3}$$

REFERENCES

1. Krebs, Richard P.; Winch, David M.; and Lieblein, Seymour: Analysis of a Megawatt Level Direct Condenser-Radiator. Progress in Astronautics and Aeronautics. Vol. 11 - Power Systems for Space Flight, M. A. Zipkin and R. N. Edwards, eds., Academic Press, Inc., 1963, pp. 475-504.

2. Haller, Henry C.; Wesling, Gordon C.; and Lieblein, Seymour: Heat-Rejection and Weight Characteristics of Fin-Tube Space Radiators with Tapered Fins. NASA TN D-2168, 1964.

3. Koestel, Alfred, and Smith, Cameron M.: Radiator Design Limitations for Dynamic Converters. Paper presented at Sixth AGARD Combustion and Propulsion Colloquium - Energy Sources and Energy Conversion, Cannes (France), Mar. 16-20, 1964.

4. Krebs, Richard P.; Haller, Henry C.; and Auer, Bruce M.: Analysis and Design Procedures for a Flat, Direct-Condensing, Central Finned-Tube Radiator. NASA TN D-2474, 1964.

5. Saule, Arthur V.; Krebs, Richard P.; and Auer, Bruce M.: Design Analysis and General Characteristics of Flat-Plate Central-Fin-Tube Sensible-Heat Space Radiators. NASA TN D-2839, 1965.

6. Denington, R. J.; Koestel, A.; Saule, A. V.; Stevens, G. T.; and Taylor, R. B.: Space Radiator Study. Rept. No. ER-4544, Thompson Ramo Wooldridge, Inc., 196[illegible]

7. Haller, Henry C.: Comparison of Heat-Rejection and Weight Characteristics of Several Radiator Fin-Tube Configurations. NASA TN D-2385, 1964.

8. Haller, Henry C.: Analysis of a Double Fin-Tube Flat Condenser-Radiator and Comparison with a Central Fin-Tube Radiator. NASA TN D-2558, 1964.

9. Haller, Henry C.; Lieblein, Seymour; and Lindow, Bruce G.: Analysis and Evaluation of a Vapor-Chamber Fin-Tube Radiator for High-Power Rankine Cycles. NASA TN D-2836, 1965.

10. Allingham, William D.; and McEntire, Jack A.: Determination of Boiling Film Coefficient for a Heated Horizontal Tube in Water-Saturated Wick Material. J. Heat Transfer (Trans. ASME), ser. C, vol. 83, no. 1, Feb. 1961, pp. 71-76.

11. Loeffler, I. J.; Lieblein, Seymour; and Clough, Nestor: Meteoroid Protection for Space Radiators. Progress in Astronautics and Aeronautics. Vol. 11 - Power Systems for Space Flight, M. A. Zipkin and R. N. Edwards, eds., Academic Press, Inc., 1963, pp. 551-579.

12. Kroeger, R.; and Grey, Jerry: A Steam Cycle Power Plant for High Power Communications Satellites. Paper presented at ASME meeting, Philadelphia (Penn.) Nov. 17-22, 1963.

13. Sparrow, E. M.; and Eckert, E. R. G.: Radiant Interaction Between Fin and Base Surfaces. J. Heat Transfer (Trans. ASME), ser. C, vol. 84, no. 1, Feb. 1962, pp. 12-18.

14. English, Robert E.; and Guentert, Donald C.: Segmenting of Radiators for Meteoroid Protection. ARS J., vol. 31, no. 8, Aug. 1961, pp. 1162-1164.

3/18/85

"The aeronautical and space activities of the United States shall be conducted so as to contribute . . . to the expansion of human knowledge of phenomena in the atmosphere and space. The Administration shall provide for the widest practicable and appropriate dissemination of information concerning its activities and the results thereof."

—NATIONAL AERONAUTICS AND SPACE ACT OF 1958

NASA SCIENTIFIC AND TECHNICAL PUBLICATIONS

TECHNICAL REPORTS: Scientific and technical information considered important, complete, and a lasting contribution to existing knowledge.

TECHNICAL NOTES: Information less broad in scope but nevertheless of importance as a contribution to existing knowledge.

TECHNICAL MEMORANDUMS: Information receiving limited distribution because of preliminary data, security classification, or other reasons.

CONTRACTOR REPORTS: Technical information generated in connection with a NASA contract or grant and released under NASA auspices.

TECHNICAL TRANSLATIONS: Information published in a foreign language considered to merit NASA distribution in English.

TECHNICAL REPRINTS: Information derived from NASA activities and initially published in the form of journal articles.

SPECIAL PUBLICATIONS: Information derived from or of value to NASA activities but not necessarily reporting the results of individual NASA-programmed scientific efforts. Publications include conference proceedings, monographs, data compilations, handbooks, sourcebooks, and special bibliographies.

Details on the availability of these publications may be obtained from:

SCIENTIFIC AND TECHNICAL INFORMATION DIVISION

NATIONAL AERONAUTICS AND SPACE ADMINISTRATION

Washington, D.C. 20546